Supplementary Information for

Frustrated $S = 1/2$ Chains in One-Dimensional Correlated Metal Ti_4MnBi_2

X. Y. Li[1]*, A. Nocera[1], K. Foyetsova[1], G. A. Sawatzky[1, 2], M. Oudah[1], N. Murai[3], M. Kofu[3], M. Matsuura[4], H. Tamatsukuri[3], and M. C. Aronson[1, 2]

[1]Stewart Blusson Quantum Matter Institute, The University of British Columbia; Vancouver BC, V6T 1Z4, Canada.

[2]Department of Physics and Astronomy, The University of British Columbia; Vancouver BC, V6T 1Z1, Canada.

[3]J-PARC Center, Japan Atomic Energy Agency; Tokai, Ibaraki 319-1195, Japan.

[4]Comprehensive Research Organization for Science and Society; Tokai, Ibaraki 319-1106, Japan.

*Corresponding author. Email: xiyang.li@ubc.ca

SUPPLEMENTARY TEXT

1. Materials and Neutron scattering

1.1 Sample preparation and characterization

Ti_4MnBi_2 single crystals were grown using the flux method described in our previous work [1]. We optimized the growth conditions to prepare large single crystals for neutron scattering experiments. The crystals are rodlike, with typical dimensions of ~1 mm × 1 mm square cross-section and ~5-10 mm in length. X-ray diffraction experiments were carried on a powder prepared from single crystals out using a Bruker D8 Advance powder x-ray diffractometer. The crystals are single phase and the expected structure was confirmed [2,3] (Fig. S1a). The crystals have shiny metallic surfaces normal to the (110) and equivalent crystal directions and the (001) crystal direction is along the rod axis (Fig. S1b). The double-sided sample used for the INS experiments (AMATERAS and DNA@J-PARC) was assembled by co-aligning ~400 crystals on both sides of two 0.3 mm thick aluminum sheets, using hydrogen-free Cytop CTL-809M as the adhesive [4] (Fig. S1c). The sample size is roughly 20 mm (width) * 30 mm (height) * 4 mm (thickness) with a total mass of 10.2 g Ti_4MnBi_2 single crystals. The (110) axis of the crystals are normal to the aluminum sheets, and the scattering plane is (*H*, *H*, *L*). The neutron diffraction peaks in the (*H*, *H*, *L*) scattering plane (including peaks projected from outside of the scattering plane) are shown in Fig. S1d, and their sharpness as well as the relatively narrow rocking curve for the sample assembly (Fig. S1e) shows that the alignment of the crystals is excellent.

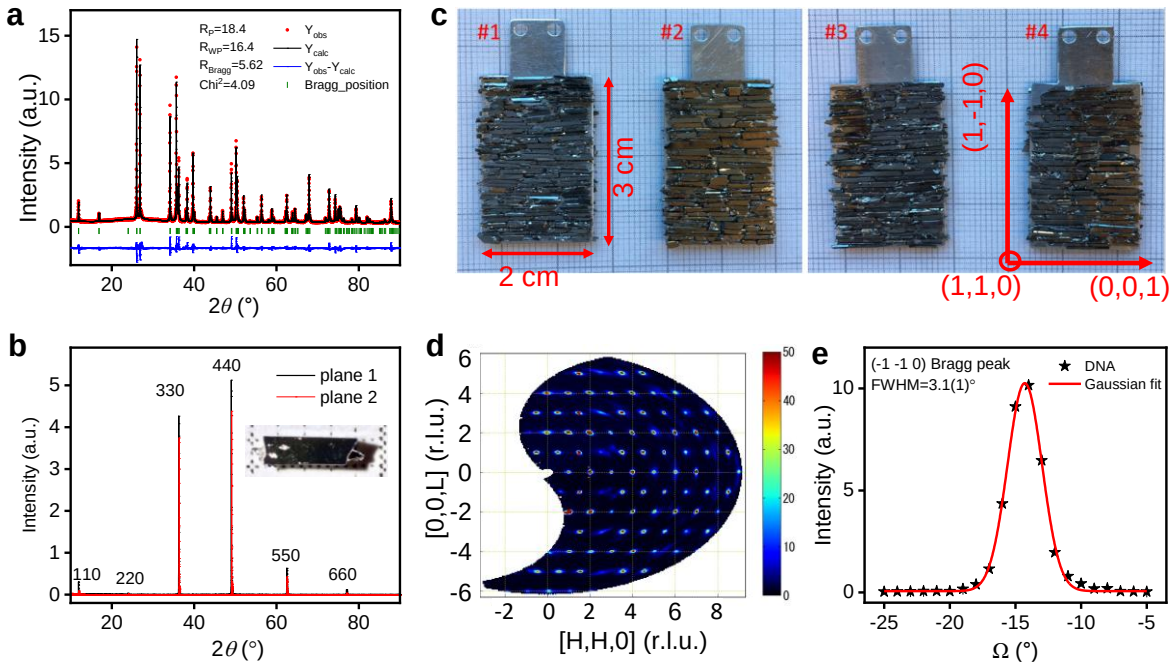

Fig. S1 | Ti_4MnBi_2 sample characterization. a, Room temperature powder x-ray diffraction data. The indicated refinement used the tetragonal structure *I*4/*mcm* (No. 140) space-group symmetry, and the refined lattice parameters are $a = b = 10.5001(1)$ Å and $c = 4.98985(8)$ Å. There are no additional Bragg

peaks that would be associated with possible impurity phases, beyond small inclusions of the flux. **b**, Surface scan of a single crystal shows the Bragg peaks associated with the (*H*, *H*, 0) and (*H*, -*H*, 0) planes. **c**, The assembly of single crystals used for neutron scattering experiments at AMATERAS@J-PARC and DNA@J-PARC, which consists of a total of four layers of Ti_4MnBi_2 crystals on both sides of two 0.3 mm thickness aluminum sheets. Individual Ti_4MnBi_2 single crystals were aligned with their (110) direction normal to the aluminum sheet, with the neutron scattering in the (*H*, *H*, *L*) plane. **d**, Elastic scattering in the (*H*, *H*, *L*) plane from AMATERAS. **e**, Neutron scattering measured rocking curve of the (-1, -1, 0) Bragg peak on Ti_4MnBi_2 sample shown in (c). The solid line is a Gaussian fit to the peak, which extracted a FWHM = 3.1(1)˚.

1.2 Inelastic neutron scattering

The 10.2 g co-aligned sample (Fig. S1c) was mounted in the (*H*, *H*, *L*) scattering plane, with the (1-10) direction vertical in the AMATERAS and DNA experiments at the MLF, J-PARC in Japan. Both experiments used the same ^{3}He cryostat sample environment with a base temperature of 0.3 K. For measurements using the direct geometry instrument AMATERAS [5], the chopper configurations were set to select multiple incident energies E_i of 3.13518, 7.73595, 15.1464, and 41.9667 meV with corresponding energy resolutions ΔE (full width at half maximum of the elastic peaks) of, respectively, 0.0581, 0.2244, 0.5652, and 2.4048 meV. The beam size was defined by slits to be 25 mm (width) * 35 mm (height), so that the sample with dimensions of 20 mm (width) * 30 mm (height) is fully illuminated by the neutron beam. The AMATERAS measurements were performed at 0.3, 1, 2, 5, 10, 25, and 100 K. The sample rotation angle is from -40˚ to 140˚ with a 0.5˚ increment at 0.3 K and a 1˚ increment at other temperatures. The data collecting time is ~ 30 hours at 0.3 K and ~ 12 hours at other temperatures. The initial data reduction was completed using the software suite UTSUSEMI [6]. The AMATERAS detectors are position sensitive along the vertical direction, which provides access to the out-of-plane (*H*, -*H*, *L*) direction and allows isolating contributions from the (*H*, *H*, *L*) scattering plane. The neutron absorption correction, including both in-plane and out-of-plane directions, was carried out using Mslice/DAVE [7], including the absorption cross section, as well as the coherent and incoherent scattering cross sections. Details of the absorption corrections follow in the next section.

For the inverse geometry instrument DNA [8], the chopper configurations were set to high-resolution mode with E_f = 2.08 meV with energy resolution of ΔE = 0.004 meV (full width at half maximum of the elastic peaks) which can measure -0.03 meV < E < 0.1 meV range. The beam size was 20 mm (width) * 30 mm (height), well matched to the sample size. The measurements were performed at 0.3, 1, 1.4, 2, and 5 K, respectively. The sample rotation angle is from -40˚ to 140˚ with 1˚ increment, and the data collecting time is ~ 24 hours, except for the 5 K data, which were measured from -40˚ to -19˚ with 1˚ increment. The data reduction and analysis were completed using the software suite UTSUSEMI [6] as well as Mslice/DAVE and PAN/DAVE [7].

A standard vanadium sample was measured under the same instrumental setup in both AMATERAS and DNA experiments, which allows us to report results in terms of absolute units, as shown below.

2. Data Analysis and Corrections

2.1 Absorption correction

Correcting for absorption effects is critical in Ti_4MnBi_2, both because of the large absorption cross sections for neutrons (Table S1), and the slab-like sample geometry (Fig. S1c). The Ti and Mn atoms have relatively large neutron absorption cross sections (Table S1). We will use the approach outlined in Wu *et al* [9] and Mantid website [10] in our treatment of the absorption, as well as in subsequent steps of normalization that allow us to express the scattering in absolute units.

Table S1: Neutron scattering and absorption cross sections for Ti, Mn, and Bi [11].

	σ_{coh} / barn	σ_{inc} / barn	σ_a / barn
Ti	1.485	2.87	6.09
Mn	1.75	0.4	13.3
Bi	9.148	0.0084	0.0338

Note: 1 barn = 10^{-24} cm^2. σ_a is absorption cross section for 2200 m/s ($\lambda = 1.7982$ Å) neutrons.

We will disregard the effects of the aluminum sheets in the sample holder, since their mass is very small compared to that of the sample.

Neutron scattering events are characterized by two distances: l_1 is the distance traveled in the sample before scattering, and l_2 represents the length traveled by the neutron after scattering. Following Mantid [10] the number of neutrons per unit solid angle scattered once by a volume element dV of the sample is given by:

$$dI_1(\theta) = J_0 \rho \frac{d\sigma}{d\Omega}(\theta) e^{-\mu(\lambda_1) l_1 - \mu(\lambda_2) l_2} dV \qquad (S1)$$

where J_0 is the incident beam flux, ρ is the atomic number density, $\frac{d\sigma}{d\Omega}(\theta)$ is the differential cross-section, and λ_1 and λ_2 are the incident and scattered neutron wavelengths. The linear attenuation coefficient μ is determined from the sum of the neutron scattering cross section σ_s, which includes both the coherent and incoherent cross sections, and σ_a, which is the neutron absorption cross section (Table S1).

$$\mu = \rho \sigma_t = \rho(\sigma_s + \sigma_a) \qquad (S2)$$

Given that the incident neutron energy for the AMATERAS experiment E_i = 3.13518 meV is low, we will omit the coherent cross section from our determination of μ.

The wavelength λ dependence of the absorption cross section is given by:

$$\sigma_a(\lambda) = \sigma_a(\lambda = 1.7982\text{Å})\left(\frac{\lambda}{1.7982}\right) \qquad (S3)$$

Although the dimensions of the sample are 20 mm (width) * 4 mm (thickness), the overall shape of the sample for the AMATERAS with E_i = 3.13518 meV can be approximated by a rectangle of width 13 mm along the crystal (001) direction, and thickness 1.6 mm along the crystal (110) direction which is perpendicular to the sample holder surface with the sample density fixed to the crystallographic density.

For the DNA data, the overall effective size has been tuned since the instrument is an inverse geometry with E_f = 2.08 meV. The absorption corrections for both AMATERAS and DNA data have been carried out using the absorption correction option with both in-plane and out-of-plane data corrected using the Mslice/DAVE analysis software package [7].

Figure S2 shows the effect of absorption on the AMATERAS measurements and demonstrates the extent to which the data can be corrected for absorption.

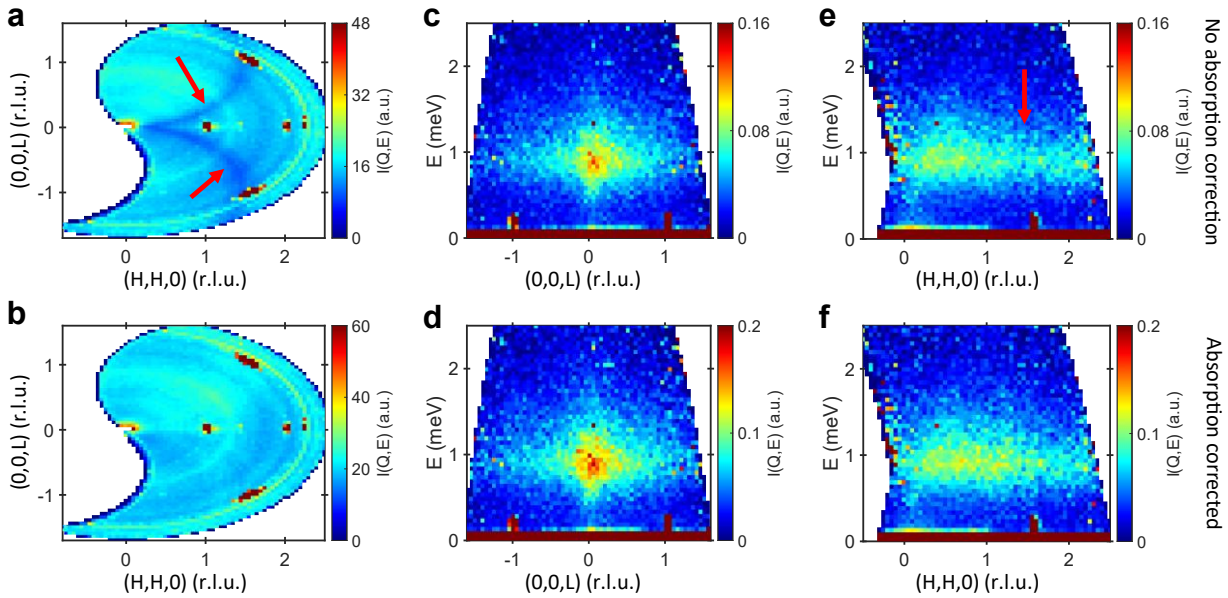

Fig. S2 | Effect of neutron absorption in Ti_4MnBi_2 AMATERAS data. **a**, **b**, Plots of the 0.3 K elastic scattering in the (*H*, *H*, *L*) scattering plane averaged within the ranges of *E* = [-0.2, 0.2] meV and (*H*, -*H*, 0) = [-0.5, 0.5] r.l.u. before (a) and after (b) the absorption correction has been applied. The blue arcs in (a) occur when the neutron beam is parallel to the (001) direction, where the neutron path length in the sample is the longest and absorption consequently the largest. This effect is practically absent in (b). **c**, **d**, Contour plots of the energy dependencies of the neutron scattering intensity, *I*(***Q***, *E*), along the (0, 0, *L*) direction with (*H*, *H*, 0) = [0, 2] r.l.u. and (*H*, -*H*, 0) = [-0.5, 0.5] r.l.u. measured at 0.3 K before (c) and after (d) the absorption correction. **e**, **f**, Contour plots of the energy dependencies of the neutron scattering intensity, *I*(***Q***, *E*), along the (*H*, *H*, 0) direction with (0, 0, *L*) = [-1, 1] r.l.u. and (*H*, -*H*, 0) = [-0.5, 0.5] r.l.u. measured at 0.3 K before (e) and after (f) the absorption correction. The red arrows in (a) and (e) point to the most apparent absorption areas.

2.2 Absolute normalization

We will next normalize both the AMATERAS and DNA data sets to absolute units. According to Xu *et al* [12] and Wu *et al* [9], there are four ways to carry out the absolute unit normalization:

1) Using the incoherent elastic scattering of a standard vanadium sample.

2) Using the incoherent elastic scattering of the sample. Since the incoherent scattering of Bi and Mn is very small (Table S1), the overall incoherent scattering is likely to be overwhelmed by the elastic scattering background.

3) Using the phonon scattering of the sample. However, it is not available for Ti_4MnBi_2.

4) Using the nuclear Bragg peaks of the sample. In practice, extinction in Bragg peak scattering can significantly affect the absolute Bragg peak intensities in single crystal experiments, and a thorough understanding of the instrument resolution is required.

We will use the incoherent elastic scattering of the standard vanadium sample method. A standard vanadium sample has been measured under the same instrumental setup both in AMATERAS and in DNA experiments.

Following Xu *et al* [12] the measured INS intensity can be written as:

$$I(\boldsymbol{Q},E) = \int \frac{d^2\sigma}{d\Omega_0 dE_0} R(\boldsymbol{Q_0},E_0,\boldsymbol{Q},E) d\boldsymbol{Q_0} dE_0 \qquad (S4)$$

where $R(\boldsymbol{Q_0},E_0,\boldsymbol{Q},E)$ is the instrument resolution function mainly determined by the instrumental setup, $\boldsymbol{Q}$ and E are the neutron wave vector and energy transfer.

For an experiment with unpolarized neutrons, the coherent magnetic scattering can be written as:

$$\frac{d^2\sigma}{d\Omega dE} = N\frac{k_f}{k_i}\left(\frac{\gamma r_0}{2}\right)^2 g^2 f^2(\boldsymbol{Q}) e^{-2W} \sum_{\alpha,\beta}\left(\delta_{\alpha,\beta} - \overrightarrow{\boldsymbol{Q_\alpha}}\cdot\overrightarrow{\boldsymbol{Q_\beta}}\right) S^{\alpha,\beta}(\boldsymbol{Q},E) \qquad (S5)$$

where N is the total number of the unit cells, $(\gamma r_0)^2 = 0.291\times10^{-24}\ cm^2 = 0.291\ barn$ with r_0 is the classical electron radius and γ is the magnetic moment of the neutron in nuclear magnetons, g is the Landé g-factor, $f(\boldsymbol{Q})$ is the magnetic form factor, e^{-2W} is the Debye-Waller factor, which at the low temperatures and small wave vectors of our measurements is taken to be unity, α and β denote the Cartesian coordinates, x, y, or z, which characterize the polarization of magnetic fluctuations. $\overrightarrow{\boldsymbol{Q_\alpha}} = \boldsymbol{Q_\alpha}/\boldsymbol{Q}$ and $\overrightarrow{\boldsymbol{Q_\beta}} = \boldsymbol{Q_\beta}/\boldsymbol{Q}$ are the projections of the unit vector along the wave vector transfer direction onto the Cartesian axes, and $S^{\alpha,\beta}(\boldsymbol{Q},E)$ is the dynamic structure

factor. The k_f/k_i calibration that is related to the incident neutron flux and scattering neutron flux is corrected for during the data reduction phase using UTSUSEMI [6].

The measured INS intensity can be written as:

$$I(\boldsymbol{Q},E) \approx N\left(\frac{\gamma r_0}{2}\right)^2 g^2 f^2(\boldsymbol{Q}) e^{-2W} \sum_{\alpha,\beta}\left(\delta_{\alpha,\beta} - \overrightarrow{\boldsymbol{Q_\alpha}}\cdot\overrightarrow{\boldsymbol{Q_\beta}}\right) S^{\alpha,\beta}(\boldsymbol{Q},E)\, R_0(\boldsymbol{Q},E) \qquad (S6)$$

where $R_0(\boldsymbol{Q},E) = \int R(\boldsymbol{Q_0},E_0,\boldsymbol{Q},E)d\boldsymbol{Q_0}dE_0$ is the resolution volume, which varies depending on the instrument setup. Thus, one can ultimately write down:

$$S(\boldsymbol{Q},E) = \sum_{\alpha,\beta}\left(\delta_{\alpha,\beta} - \overrightarrow{\boldsymbol{Q_\alpha}}\cdot\overrightarrow{\boldsymbol{Q_\beta}}\right) S^{\alpha,\beta}(\boldsymbol{Q},E) = \frac{13.75(barn^{-1})I(\boldsymbol{Q},E)}{Ng^2 f^2(\boldsymbol{Q}) e^{-2W} R_0(\boldsymbol{Q},E)} \qquad (S7)$$

where $S(\boldsymbol{Q},E)$ has units of meV^{-1}. The magnetic dynamic structure factor can be further written as:

$$M(\boldsymbol{Q},E) = g^2\mu_B^2 f^2(\boldsymbol{Q}) S(\boldsymbol{Q},E) = \frac{13.75(barn^{-1})\mu_B^2 I(\boldsymbol{Q},E)}{N e^{-2W} R_0(\boldsymbol{Q},E)} \qquad (S8)$$

which has the units of $\mu_B^2\cdot$meV^{-1}.

The $\boldsymbol{Q}$-dependent magnetic susceptibility, $\chi''(\boldsymbol{Q}, E)$, is related to the magnetic dynamic structure factor, $M(\boldsymbol{Q}, E)$, by the principle of detailed balance, leading to:

$$\chi''(\boldsymbol{Q},E) = \pi\left[1 - e^{-\frac{E}{k_B T}}\right] M(\boldsymbol{Q},E) \qquad (S9)$$

where $\left[1 - e^{-\frac{E}{k_B T}}\right]$ describes the Bose-Einstein statistics, k_B is the Boltzmann constant, and T is the temperature.

The Landé g-factor, magnetic form factor, and Debye-Waller factor are sample dependent, and can be estimated. For instance, the Curie-Weiss fitting suggested $g \approx 2$ (Fig. S9). The Debye-Waller factor $e^{-2W} \approx 1$ at low temperatures and small $\boldsymbol{Q}$, and $f(\boldsymbol{Q})$ is the magnetic form factor which can be calculated by DFT or estimated by fitting the INS data (Fig. S15). Thus, to complete the absolute unit calibration, one needs to know the resolution volume $R_0(\boldsymbol{Q},E)$, which can be calculated using the incoherent elastic scattering data of the standard vanadium sample. The cross-section for incoherent elastic scattering is:

$$\left(\frac{d\sigma}{d\Omega}\right)_{inc,el} = \frac{N}{4\pi}\sum_j \sigma_j^{inc,V} e^{-2W} \qquad (S10)$$

where $\sigma_j^{inc,V} = 5.08\ barn$ is the incoherent neutron scattering cross-section of the j^{th} vanadium atom [11]. So, from the standard vanadium sample measured scattering intensity, one can get:

$$\int I(\boldsymbol{Q},E)dE = \frac{N}{4\pi}\sum_j \sigma_j^{inc,V} e^{-2W} R_0(\boldsymbol{Q},E) \qquad (S11)$$

Thus, the resolution volume $R_0(\boldsymbol{Q},E)$, can be calculated as:

$$R_0(\boldsymbol{Q},E) = \frac{4\pi \int I(\boldsymbol{Q},E)dE}{N\sum_j \sigma_j^{inc,V} e^{-2W}} \qquad (S12)$$

For the AMATERAS experiment, a 1.5397 g standard vanadium sample was measured at room temperature with a total counting time of about 8 hours. Thus, the measured resolution volume of the AMATERAS setup is:

$$R_0(\boldsymbol{Q},E)_{AMATERAS} = \frac{4\pi \int I(\boldsymbol{Q},E)_{V,AMATERAS}dE}{N\sum_j \sigma_j^{inc,V} e^{-2W}} = 1.082\times 10^{-21}\frac{meV}{barn} \qquad (S13)$$

For the DNA experiment, a 5.5666 g standard vanadium sample was measured from 7 to 4.5 K with a total counting time of about 7 hours. Thus, the measured resolution volume of the DNA setup is:

$$R_0(\boldsymbol{Q},E)_{DNA} = \frac{4\pi \int I(\boldsymbol{Q},E)_{V,DNA}dE}{N\sum_j \sigma_j^{inc,V} e^{-2W}} = 5.640\times 10^{-25}\frac{meV}{barn} \qquad (S14)$$

Finally, the resolution volume $R_0(\boldsymbol{Q},E)$ values and Eq. S8 can be used together to express the INS data of the Ti_4MnBi_2 sample in absolute units.

The large incoherent scattering cross section of the vanadium causes the above normalization process to ignore the incoherent elastic scattering background from the sample environment.

2.3 Temperature-independent background subtraction

The INS measured data can be separated into temperature-dependent and temperature-independent parts, where the temperature-dependent part obeys the principle of detailed balance. In contrast, the temperature-independent scattering, including the resolution broadened elastic scattering tails and the sample environment's scattering, can be approximated as being temperature independent at sufficiently low temperatures. Following Hong *et al* [13], the measured INS raw data intensity $I_r(E,\ T_1)$ at temperature T_1 for any specific $\boldsymbol{Q}$ can be written as:

$$I_r(E,\ T_1) = B(E) + I(E,T_1) \qquad (S15a)$$

$$I_r(-|E|,\ T_1) = B(-|E|) + I(|E|,T_1)e^{-\frac{|E|}{k_B T_1}} \qquad (S15b)$$

where $B(E)$ is the temperature-independent background, and $I(E,T_1)$ is the INS intensity that obeys detailed balance. By measuring the sample at another temperature T_2, two additional equations can be written as:

$$I_r(E,\ T_2) = B(E) + I(E,T_2) \qquad (S16a)$$

$$I_r(-|E|,\ T_2) = B(-|E|) + I(|E|,T_2)e^{-\frac{|E|}{k_B T_2}} \qquad (S16b)$$

The temperature-dependent and the temperature-independent parts of the raw data intensity can be determined by solving these four equations simultaneously. Solving for the temperature-independent background gives:

$$B(E) = \frac{I_r(E,\ T_1)e^{-\frac{|E|}{k_B T_1}} - I_r(-|E|,\ T_1) + I_r(-|E|,\ T_2) - I_r(E,\ T_2)e^{-\frac{|E|}{k_B T_2}}}{e^{-\frac{|E|}{k_B T_1}} - e^{-\frac{|E|}{k_B T_2}}} \qquad (S17a)$$

$$B(-|E|) = \frac{I_r(E,\ T_1)e^{-\frac{|E|}{k_B T_1}-\frac{|E|}{k_B T_2}} - I_r(-|E|,\ T_1)e^{-\frac{|E|}{k_B T_2}} + I_r(-|E|,\ T_2)e^{-\frac{|E|}{k_B T_1}} - I_r(E,\ T_2)e^{-\frac{|E|}{k_B T_1}-\frac{|E|}{k_B T_2}}}{e^{-\frac{|E|}{k_B T_1}} - e^{-\frac{|E|}{k_B T_2}}} \qquad (S17b)$$

This method works well when the energy dependence of the energy resolution can be ignored. In the analysis of the AMATERAS data, we used the data sets measured at T_1 = 0.3 K and T_2 = 100 K to determine the temperature-independent background, which is subsequently subtracted from the data measured at all other temperatures. The effects of background subtraction are demonstrated in Fig. S3.

Since the phonon density of states follows the Bose distribution, one can further subtract the phonon contribution in order to isolate the magnetic part of the scattering. The phonon density of states should be the same at low and high temperatures once the data have been corrected for the Bose factor. Using Eq. S15 and Eq. S16,

$$I(|E|,T_1)_{subtract\ phonon} = \left[I(|E|,T_1)\left(1 - e^{-\frac{|E|}{k_B T_1}}\right) - I(|E|,T_2)\left(1 - e^{-\frac{|E|}{k_B T_2}}\right)\right] \Big/ \left(1 - e^{-\frac{|E|}{k_B T_1}}\right)$$

$$= [I_r(E,\ T_1) - I_r(-|E|,\ T_1) + I_r(-|E|,\ T_2) - I_r(E,\ T_2)] \Big/ \left(1 - e^{-\frac{|E|}{k_B T_1}}\right) \qquad (S18)$$

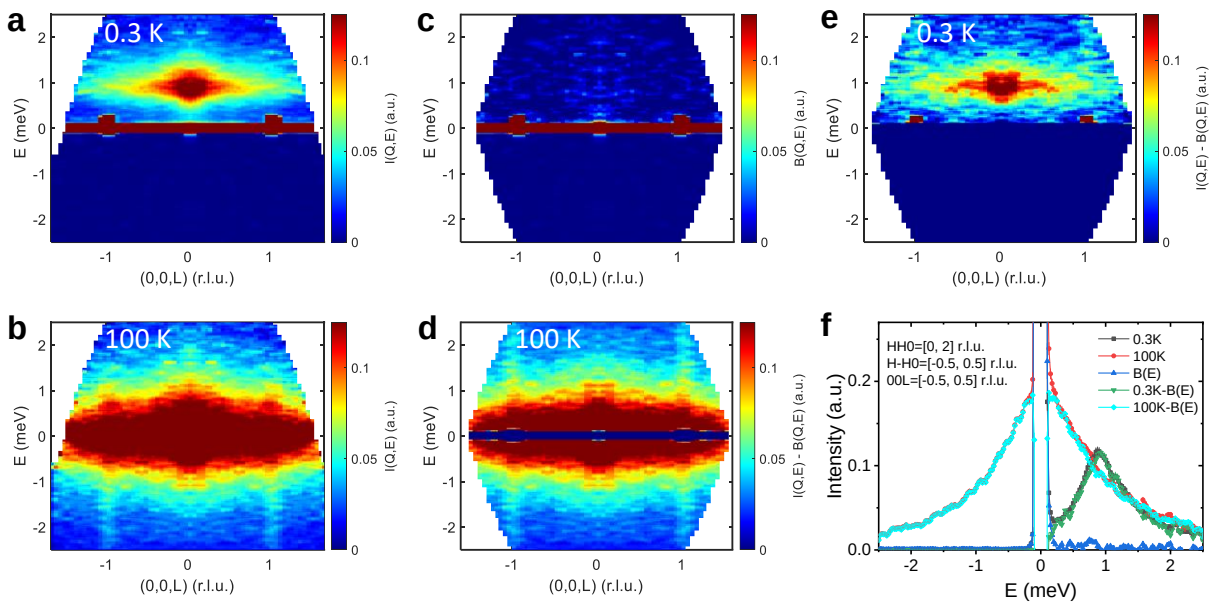

Fig. S3 | Temperature-independent background subtraction in Ti_4MnBi_2. **a**, **b**, The INS intensity $I(\boldsymbol{Q}, E)$ measured at 0.3 K (a) and 100 K (b) at AMATERAS. The data are averaged over the ranges of (H, H, 0) = [0, 2] r.l.u. and (H, -H, 0) = [-0.5, 0.5] r.l.u. **c**, The temperature-independent background $B(\boldsymbol{Q}, E)$ was calculated using the 0.3 K and 100 K data. Compared with the raw data shown in (a) and (b), the intensity of $B(\boldsymbol{Q}, E)$ is quite weak. **d**, **e**, Data plots at 100 K (d) and 0.3 K (e) from which the temperature-independent background has been subtracted. **f**, The 1D plots of the raw data, temperature-independent $B(E)$ data, and temperature-independent background subtracted data, averaged over the ranges of (H, H, 0) = [0, 2] r.l.u., (H, -H, 0) = [-0.5, 0.5] r.l.u., and (0, 0, L) = [-0.5, 0.5] r.l.u. The plots show that the subtraction of the temperature-independent background for the energies E = [0.5, 1.5] meV that is dominated by the spinon continuum reduces the raw intensity by less than 4%.

Using Eq. S18 and Eq. S8 allows the calculation of the phonon subtracted $M(\boldsymbol{Q}, E)$, and the effect of subtracting it from the temperature-independent background subtracted data at 0.3 K is demonstrated in Fig. S4. The comparison of $M(\boldsymbol{Q}, E)$ at 0.3 K with and without the phonon subtraction is shown in Fig. S4. We should note that the 100 K data has some residual magnetic scattering, which is also subtracted in the above analysis. However, the phonon subtraction around the Bragg peaks (0, 0, 1) and (0, 0, -1) should not be affected.

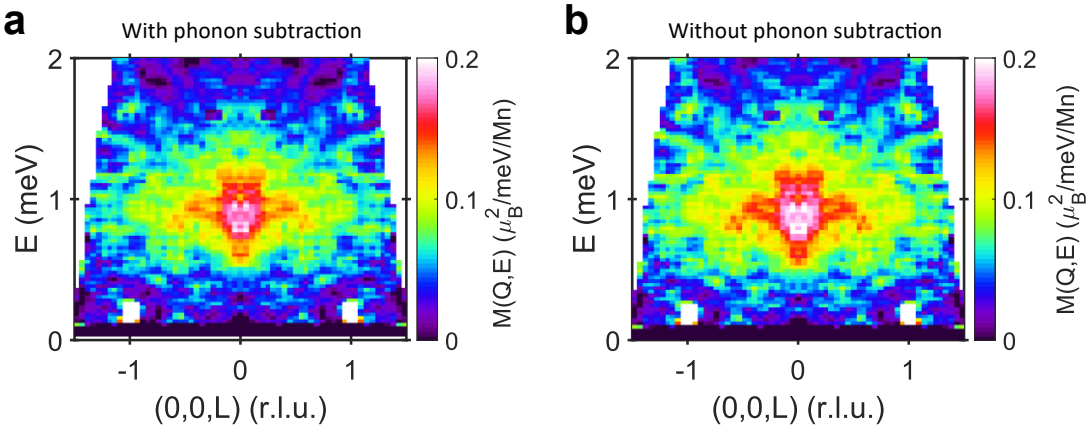

Fig. S4 | Phonon subtraction in Ti_4MnBi_2. **a**, **b**, The INS $M(\boldsymbol{Q}, E)$ measured at 0.3 K with phonon scattering subtracted (a) using the 100 K data, and without phonon subtraction (b) plots. The data are averaged over the ranges of (H, H, 0) = [0, 2] r.l.u. and (H, -H, 0) = [-0.5, 0.5] r.l.u. The comparison of (a) and (b) suggests that phonon scattering is not significant at 0.3 K.

2.4 Magnetic moment sum rule

We will use the approach outlined in Wu *et al* [9] to describe and calculate the moment sum rule in Ti_4MnBi_2. The sum rule of the dynamic spin correlation function $S^{\alpha,\beta}(\boldsymbol{Q}, E)$ is satisfied when integrated over the first Brillouin zone (BZ):

$$\frac{\sum_{\alpha,\beta}\int_{-\infty}^{+\infty}\int_{BZ}^{1st} S^{\alpha,\beta}(\boldsymbol{Q},E)\,d\boldsymbol{Q}dE}{\int_{BZ}^{1st} d\boldsymbol{Q}} = S(S+1)\delta_{\alpha,\beta} \qquad (S19)$$

The energy E integration excludes elastic scattering, which is presumably dominated by different sources of elastic scattering, apart from magnetic scattering. For an S = 1/2 system, the sum rule is a combination of three independent sum rules, one for each polarization:

$$\frac{\int_{-\infty}^{+\infty}\int_{BZ}^{1st} S^{\alpha,\alpha}(\boldsymbol{Q},E)\,d\boldsymbol{Q}dE}{\int_{BZ}^{1st} d\boldsymbol{Q}} = \frac{1}{3}S(S+1)\delta_{\alpha,\alpha} = \frac{1}{4}, \qquad \alpha = x,y,z \qquad (S20)$$

The data normalized to absolute units can be used to verify the sum rules in Ti_4MnBi_2.

The integrated M^2_{Fluct} shown in Fig. 4c is calculated by:

$$M^2 = \frac{\int_{-\infty}^{+\infty}\int_{BZ}^{1st} \frac{M(\boldsymbol{Q},E)}{f^2(\boldsymbol{Q})}\,d\boldsymbol{Q}dE}{\int_{BZ}^{1st} d\boldsymbol{Q}} \qquad (S21)$$

with the data integrated in E = [-2.4, 2.4] meV range (the elastic incoherent scattering range of [-0.1, 0.1] meV has been excluded) and $\boldsymbol{Q}$ averaged in the first BZ. A factor of 3/2 is included in

Fig. 4c, intended to represent the contribution from the longitudinal dynamic structure factor $S_{zz}(\boldsymbol{Q}, E)$, which is nearly absent in the measured and calculated $S(\boldsymbol{Q}, E)$, due to the easy axis character of Ti_4MnBi_2 (see sections 4.2 and 4.5).

The elastic moment M^2_{Elas} shown in Fig. 4c is calculated using Eq. S21 with the data integrated over E = [-0.1, 0.1] meV and $\boldsymbol{Q}$ averaged over (0, 0, L) = [0, 1] r.l.u., (H, H, 0) = [-0.5, 0.5] r.l.u., and (H, -H, 0) = [-0.5, 0.5] r.l.u., where the strongest magnetic diffuse scattering is found (Figs. 2a-d). The 100 K data are used as a background, which slightly underestimates the magnetic signal, due to a very small residual magnetic signal at 100 K. The largest uncertainty affecting the moment sum rule is the lack of an expression for the magnetic form factor that is valid for all measured wave vectors. The data presented in Fig. 4c include a Lorentzian form factor that is, strictly speaking, most accurate for wave vectors $\boldsymbol{Q}_L < 0.7$ r.l.u. The discussion of Fig. S15 shows that the Lorentzian form factor underestimates the form factor for these larger values of $\boldsymbol{Q}_L$, and consequently the values of M^2_{Elas} in Fig. 4c are somewhat inflated.

2.5 Static magnetic susceptibility and the Kramers-Kronig relation

As described in Enderle *et al* [14], the imaginary part of the dynamic susceptibility is directly related to the static susceptibility. The fluctuation-dissipation theorem gives the relationship between $S^{\alpha,\beta}(\boldsymbol{Q}, E)$ and $\chi^{\alpha,\beta''}(\boldsymbol{Q}, E)$ as [14,15]:

$$\chi^{\alpha,\beta''}(\boldsymbol{Q}, E) = \pi g^2 \mu_B^2 f^2(\boldsymbol{Q}) \left(1 - e^{-\frac{E}{k_B T}}\right) S^{\alpha,\beta}(\boldsymbol{Q}, E) \quad (S22)$$

$\chi^{\alpha,\beta''}(\boldsymbol{Q}, E)$ is related to the bulk susceptibility via the Kramers-Kronig relation:

$$\chi^{\alpha,\beta'}(\boldsymbol{Q}, 0) = \frac{1}{\pi} \int dE \frac{1}{E} \chi^{\alpha,\beta''}(\boldsymbol{Q}, E) = g^2 \mu_B^2 f^2(\boldsymbol{Q}) \int_{-k_B T}^{E_{cutoff}} dE \frac{1}{E} \left(1 - e^{-\frac{E}{k_B T}}\right) S^{\alpha,\beta}(\boldsymbol{Q}, E) \quad (S23)$$

The bulk susceptibility is measured in a magnetic field that is applied along one direction in single crystal, which gives $\chi^{\alpha,\alpha'}(\boldsymbol{Q} = 0, 0)$ with $\alpha = x, y, z$.

The integrated INS measured susceptibility [16] shown in Fig. 4e is calculated using the following expression:

$$\frac{1}{\pi} \int_{-k_B T}^{E_{cutoff}} dE \frac{1}{E} \chi''(\boldsymbol{Q}, E)$$

where the energy integration is carried out over the energy range E = [-$k_B T$, 2.4] meV range, excluding the elastic incoherent scattering with energies in the range [-0.1, 0.1] meV where $\chi''(E)$ is not known. The average of $\chi''(\boldsymbol{Q}, E)$ within the first BZ is used to approximate $\chi''(\boldsymbol{Q} = 0, E)$. Comparing the high temperatures data, an adjustment scaling factor is applied to estimate the intensity attenuation at large $\boldsymbol{Q}$ due to the form factor.

3. First-principles Density-functional Theory (DFT) Calculations

The DFT calculations of the electronic structure of Ti_4MnBi_2 were performed using the augmented plane-wave all-electron package WIEN2k [17] and the gradient-corrected local density approximation (GGA) by Perdew, Burke, and Ernzenhof [18] for the energy functional. The basis set size is set by choosing RKmax = 7.0, while the BZ integration is performed using a Γ-centered 10 × 10 × 10 *k*-vector grid. The considered structural model of Ti_4MnBi_2 is based on the experimentally determined tetragonal unit cell with the space group *I*4/*mcm* and the lattice vectors equal to $a = b = 10.547214$ Å and $c = 4.974468$ Å [2,3]. In addition to the non-spin-polarized calculations that have been performed to obtain the Mn 3*d* projected densities of states presented in Fig. 1b, we also carried out two spin-polarized calculations, one corresponding to a ferromagnetic (FM) ordering of the molecular orbital (MO) [19] spins and one corresponding to their nearest-neighbor antiferromagnetic (AF) ordering. The spatial distribution of the spin density in the latter solution is presented in Fig. 1f, clearly demonstrating the MO character of the localized magnetic moments in Ti_4MnBi_2, related to experimental and theoretical work identifying magnetic MOs in MnSi [19]. The AF solution is by about 8 meV per Mn higher in energy compared with the FM solution, confirming that the nearest-neighbor spin coupling J_1 in our J_1-J_2 Hamiltonian is FM. We note, however, that our simple GGA approach is likely to significantly underestimate correlate ion effects associated with the localized MO magnetic moments so that the realistic J_1 value may be quite different from the one that one might deduce from the 8 meV energy difference given by GGA. Unfortunately, the DFT+U method [20] which is often used to improve the treatment of local correlation effects in DFT, cannot be applied to Ti_4MnBi_2 because of its known tendency to destroy MOs [21]. As a result of underestimated correlations, both spin-polarized GGA solutions were found to be very difficult to converge, for which reason we found it helpful to turn off spatial symmetrization (by setting the space group to P1) and to run spin-orbit (SO) coupled calculations with the SO coupling artificially set to zero in order to disable any additional internal symmetrization done by WIEN2k.

The Sommerfeld coefficient γ_{DFT} was calculated using the expression [22]:

$$\gamma_{DFT} = \frac{\pi^2}{3} k_B^2 D(E_F) \qquad (S24)$$

where $D(E_F)$ is the density of states at the Fermi level E_F in the FM DFT solution in which only the itinerant electronic states contribute. $D(E_F)$ was obtained to be equal to 10.7 states/($V_{u.c.}$-eV) or 9.74×10^{47} states/(m^3-J).

4. Density Matrix Renormalization Group (DMRG)

4.1 Details of DMRG calculations and ground state phase diagram from DMRG

The DMRG method is widely recognized as the best numerical method to solve for the ground state of one-dimensional spin chains beyond the means of exact diagonalization methods. It is variationally exact for ground state calculations, as the accuracies of ground state energies and gap to the first excited state can be improved by increasing the so-called "bond-dimension" parameter, which encapsulates the expressivity of the Matrix Product State (MPS) wave-function ansatz underlying the method. For the calculation of spectral functions, such as the dynamical spin structure factor, DMRG calculations are again variationally exact, but there are a few additional and important limitations depending on the approach used. Dynamical spin structure factors are defined as two-point, two-times spin-spin correlators, which are eventually space-time Fourier Transformed to the momentum-energy domain.

While DMRG calculations are usually performed in real space, requiring a single space Fourier Transform, there are two methods to evaluate spectral functions in the energy domain. The first is to use the time evolution and then Fourier transform to the energy domain. This has the main drawback of requiring long time evolutions to be able to perform a reliable time Fourier transform. Besides requiring an increasing bond-dimension as a function of time, the time evolution must be truncated resulting in an extrinsic broadening of the spectral peaks in energy. The second method, which we adopt in our work, is to evaluate the dynamical structure factor directly in the energy domain, and repeating the calculation for each energy slice in a pre-determined energy interval (this can be done trivially in parallel in standard computing cluster facilities). This second method introduces explicitly an extrinsic broadening parameter, which however can be matched to the energy resolution of the INS experiment.

In summary, there are essentially four sources of error for the evaluation of the spectral function using the DMRG method:
1) finite bond-dimension parameter to converge the ground state energy and MPS approximation for the wave-function $|\Psi>$.
2) finite bond-dimension parameter to converge the two-point correlator resolvent at fixed Energy = E^* and related Krylov expansion error [28].
For both 1) and 2), we have checked that our results are converged with respect to the bond-dimension parameter and Krylov expansion error.
3) finite precision of the space Fourier Transform in a finite size chain with open boundaries. This is usually evaluated using the so-called center-trick [28]. We have simulated chains up to $L = 200$ length, so that our results are converged in system size and representative of the thermodynamic limit.
4) finite extrinsic broadening parameter, which however can be matched to the energy resolution of the INS experiment, which is always finite.

To describe the behavior of the Ti_4MnBi_2 chain, we used the anisotropic J_1-J_2 model Hamiltonian:

$$H = J_1 \sum_{n=1}^{L-1} \left[S_n^z \cdot S_{n+1}^z + \varepsilon_1 \left(S_n^x \cdot S_{n+1}^x + S_n^y \cdot S_{n+1}^y \right) \right] + J_2 \sum_{n=2}^{L-2} \left[S_n^z \cdot S_{n+2}^z + \varepsilon_2 \left(S_n^x \cdot S_{n+2}^x + S_n^y \cdot S_{n+2}^y \right) \right] \quad (S25)$$

where J_1 and J_2 are the nearest-neighbors and next-nearest-neighbors exchange parameters while $\boldsymbol{\varepsilon}_1$ and $\boldsymbol{\varepsilon}_2$ are the magnetic anisotropic parameters dictating the easy-axis ($\boldsymbol{\varepsilon}_1 < 1$, $\boldsymbol{\varepsilon}_2 < 1$) or easy-plane ($\boldsymbol{\varepsilon}_1 > 1$, $\boldsymbol{\varepsilon}_2 > 1$) character of magnetic interactions. To compute the ground state phase diagram of the model, we simulated chains of L sites (up to 200) with open boundary conditions using the standard DMRG method [23,24] implemented in the DMRG++ code [25]. For the ground state calculations, we used up to m = 1000 DMRG states allowing for a maximum truncation error of 10^{-9}. We computed several quantities, such as the total magnetization:

$$M_a = \sum_{i=1}^{L} \frac{\langle \Psi_{gs} | S_i^a | \Psi_{gs} \rangle}{L} \quad (S26)$$

(where S_i^a is the spin operator on site i along the a = x, y, z directions), the longitudinal $M_{ij}^{/\!/}$ and transverse $M_{ij}^{\perp}$ spin-spin correlations:

$$M_{ij}^{/\!/} = \langle \Psi_{gs} | S_i^z S_j^z | \Psi_{gs} \rangle, \qquad M_{ij}^{\perp} = \langle \Psi_{gs} | S_i^+ S_j^- | \Psi_{gs} \rangle \quad (S27)$$

As in other studies [26–28], we also computed vector-chiral (VC) and quadrupolar (Q) correlations functions:

$$M_{ij}^{VC_x} = \langle \Psi_{gs} | \kappa_i^x \kappa_j^x | \Psi_{gs} \rangle \quad (S28)$$

$$M_{ij}^{VC_y} = \langle \Psi_{gs} | \kappa_i^y \kappa_j^y | \Psi_{gs} \rangle \quad (S29)$$

$$M_{ij}^{VC_z} = \langle \Psi_{gs} | \kappa_i^z \kappa_j^z | \Psi_{gs} \rangle \quad (S30)$$

$$M_{ij}^{Q} = \langle \Psi_{gs} | Q_i^+ Q_j | \Psi_{gs} \rangle \quad (S31)$$

where $\kappa_j = S_j \times S_{j+1}$ and $Q_j^+ = S_j^+ S_{j+1}^+$.

Finally, to establish the presence of FM phases, we computed the spin S of the ground state wavefunction from the standard formula:

$$\sum_{a=x,y,z} \sum_{i,j} \langle \Psi_{gs} | S_i^a S_j^a | \Psi_{gs} \rangle = S(S+1) \quad (S32)$$

where S is extracted from $S_{tot} = S(S+1)$ (Fig. S5). S can go up to $L/2$.

Let's start discuss the phase diagram of the model sketched in Fig. 1h in the main text, where the parameters are $\boldsymbol{\alpha} = J_2/|J_1|$, and $\boldsymbol{\varepsilon}_2$, and we have chosen $\boldsymbol{\varepsilon}_1 = 1$.

A. ↑↑↓↓ and polarized FM phases

For any value of the uniaxial anisotropy $\boldsymbol{\varepsilon}_2 < 1$, the most prominent feature of the phase diagram is the presence of a ↑↑↓↓ phase for sufficiently large $\boldsymbol{\alpha}$. For $\boldsymbol{\alpha} < \boldsymbol{\alpha}_c(\boldsymbol{\varepsilon}_2)$, then Fig. S5 clearly shows that the system converged to a partially polarized FM phase.

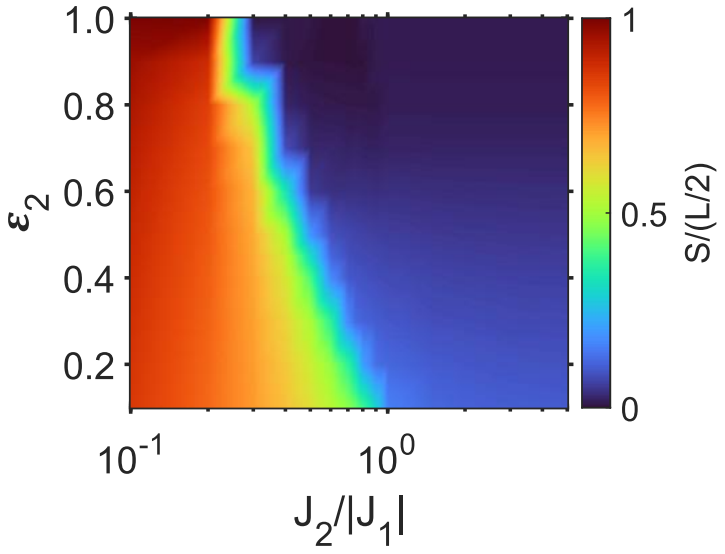

Fig. S5 | Total spin $S/(L/2)$ as functions of J_1-J_2 XXZ parameters α, ε_2 at T = 0. Based on the definition in Eq. S31, $S/(L/2)$ = 1 means fully polarized FM state. Here the chain length is L = 150 sites.

The ↑↑↓↓ phase was detected as follows: we first checked long distance behavior of the two-point correlation function $M_{ij}^{/\!/}$, which shows a ↑↑↓↓ character (see Fig. S6a). Note that a standard ↑↓ Ising order would show:

$$\lim_{|i-j|\to\infty} M_{ij}^{/\!/} = (-1)^{i+j} m_z^2 \qquad (S33)$$

where $\langle S_i^z \rangle \approx \langle S_j^z \rangle \approx m_z$.

We then defined the ↑↑↓↓ correlation function:

$$M_{ij}^{\uparrow\uparrow\downarrow\downarrow} = \langle \Psi_{gs} | D_i^z D_j^z | \Psi_{gs} \rangle, \qquad D_j^z = \frac{\left(S_{2j}^z + S_{2j+1}^z\right)}{2} \qquad (S34)$$

which shows long range order,

$$\lim_{|i-j|\to\infty} M_{ij}^{\uparrow\uparrow\downarrow\downarrow} = (-1)^{i+j} d_z^2 \qquad (S35)$$

where $\langle D_i^z \rangle \approx \langle D_j^z \rangle \approx d_z$. One can then think of $d_z = \sqrt{\left| \lim_{|i-j|\to\infty} M_{ij}^{\uparrow\uparrow\downarrow\downarrow} \right|}$ as an order parameter for the $\uparrow\uparrow\downarrow\downarrow$ phase. In a system with periodic boundary conditions, one would have expected a 4-fold degeneracy for the ground state in this case, spanned by the states,

$$|\Psi_{gs}^1\rangle = |\cdots\uparrow\uparrow\downarrow\downarrow\cdots\rangle,\ \ |\Psi_{gs}^2\rangle = |\cdots\downarrow\uparrow\uparrow\downarrow\cdots\rangle,\ \ |\Psi_{gs}^3\rangle = |\cdots\downarrow\downarrow\uparrow\uparrow\cdots\rangle,\ \ |\Psi_{gs}^4\rangle = |\cdots\uparrow\downarrow\downarrow\uparrow\cdots\rangle \tag{S36}$$

As DMRG is most efficient with open boundaries, we found only a 2-fold degenerate ground state manifold in this case. We verified numerically that open boundaries break the 4-fold degeneracy energetically favoring the states $|\Psi_{gs}^1\rangle$ and $|\Psi_{gs}^3\rangle$ which display FM bonds at the edge of the chain.

We then computed the gap $\boldsymbol{\Delta}(L)$ above this 2-fold degenerate state for different system sizes up to L = 72. Since the correlation length is known to increase substantially for $\boldsymbol{\varepsilon}_2 \to 1$, we hatched the part of the phase diagram depicted in Fig. 1h in the main text where we found harder to extrapolate to extremely small gaps at larger sizes. Fig. S6b shows the exponential decay of the transverse spin-spin correlations, $M_{ij}^{\perp}$. We finally note that the VC correlations are also exponentially decaying and therefore are short-ranged in this phase (Fig. S6c).

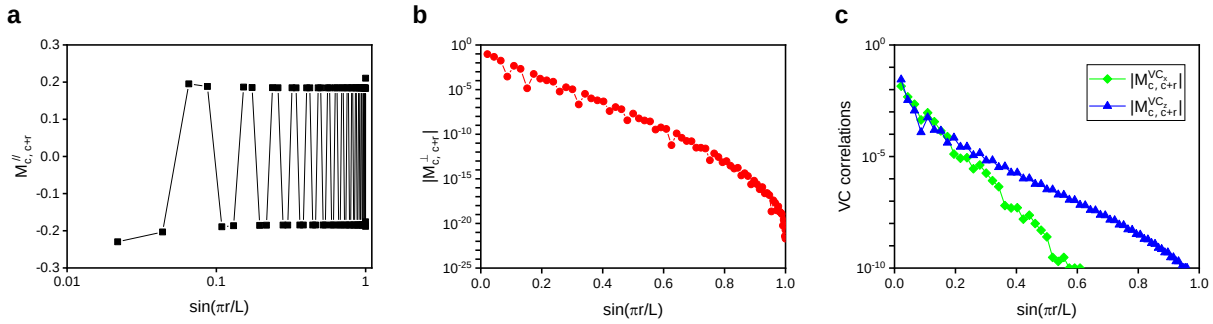

Fig. S6 | The two-point correlation function a, $M_{ij}^{/\!/}$, b, $M_{ij}^{\perp}$, and c, the VC correlations as functions of the distance *r* of the spin *c*+*r* respect the spin *c* in the chain center. These results are performed with $\boldsymbol{\alpha} = J_2/|J_1| = 0.7$ and $\boldsymbol{\varepsilon}_2 = 0.4$, which is in the $\uparrow\uparrow\downarrow\downarrow$ phase but very close to the FM $\uparrow\uparrow\downarrow\downarrow$ phase boundary. Here the chain length is L = 150 sites.

B. Vector-Chiral phase

We have found that in the region of larger $\boldsymbol{\varepsilon}_2$, and intermediate $\boldsymbol{\alpha}$ as indicated in the phase diagram in Fig. 1h in the main text, the VC correlation functions show a power law decay as a function of distance (it was difficult to distinguish a power law from an exponential with very large correlation length), which is compatible with the vanishingly small gap found in this region. Note that while the $M_{ij}^{/\!/}$ show long range order in the $\uparrow\uparrow\downarrow\downarrow$ as discussed in the previous section (see the black curve in Fig. S7b), these are exponentially decaying in the VC phase (Fig. S7a). On the other hand, both the $M_{ij}^{VC_x}$ and $M_{ij}^{VC_z}$ correlations function (green and blue curves in Fig. S7) show quasi-long range order for $\boldsymbol{\varepsilon}_2$ = 0.8 and $\boldsymbol{\alpha}$ = 0.8. In both phases, $M_{ij}^{\perp}$ and M_{ij}^{Q} (red and magenta curves in Fig. S7) are subdominant.

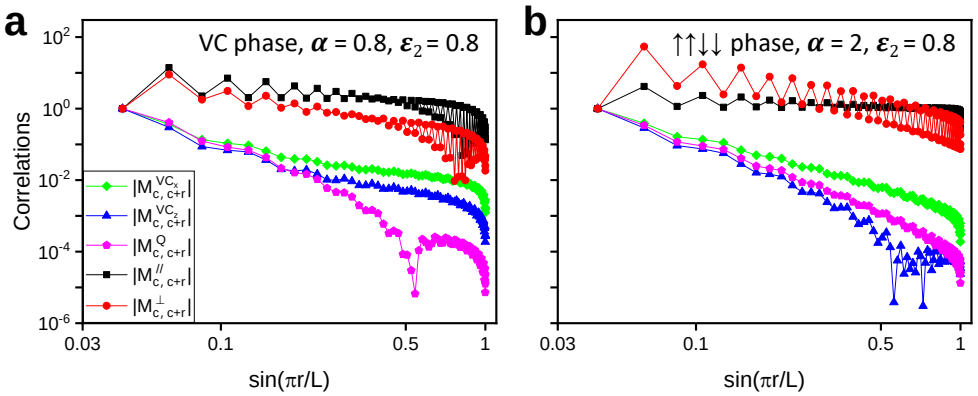

Fig. S7 | Absolute value of various correlation functions, as indicated. a, These results are performed with $\alpha = J_2/|J_1| = 0.8$ and $\varepsilon_2 = 0.8$, which is in the VC phase. **b**, These results are performed with $\alpha = J_2/|J_1| = 2$ and $\varepsilon_2 = 0.8$, which is in the ↑↑↓↓ phase. Here the chain length is $L = 150$ sites.

4.2 Dynamical spin structure factors with DMRG

We computed the longitudinal $S_{ij}^{zz}(E)$ and transverse $S_{ij}^{+-}(E)$ spin structure factors in real space:

$$S_{ij}^{zz}(E) = -\frac{1}{\pi} Im \langle \Psi_{gs} \left| S_j^z \frac{1}{E - \hat{H} + E_0 + i\eta} S_i^z \right| \Psi_{gs} \rangle \qquad (S37)$$

$$S_{ij}^{\pm}(E) = -\frac{1}{\pi} Im \langle \Psi_{gs} \left| S_j^+ \frac{1}{E - \hat{H} + E_0 + i\eta} S_i^- \right| \Psi_{gs} \rangle \qquad (S38)$$

using the DMRG correction-vector method [29,30]. The corresponding correlation functions in momentum space were then obtained by a Fourier transform. When calculating the dynamical correlation functions, we fixed the broadening coefficient to $\eta = 0.06J_2$ and computed the spectral functions for each E using the root-N Correction-Vector algorithm with Krylov decomposition and a two-site DMRG update recently introduced, as implemented in the DMRG++ code [25]. We used $N = 8$ and kept up to $m = 800$ states. To avoid the necessity of reorthogonalizing the Krylov vectors, we allowed up to 200 Krylov vectors and truncated the effective Hamiltonian decomposition with a tolerance of 10^{-12}. A representative transverse dynamic structure factor $S_{XX}(\boldsymbol{Q}, E)$ and longitudinal dynamic structure factor $S_{ZZ}(\boldsymbol{Q}, E)$ are shown in Fig. S8.

The $\boldsymbol{Q}^*$ values shown in Fig. 3f are calculated by analyzing peaks of the $S_{XX}(\boldsymbol{Q}, E)$ cut at $E = 0$, where two peaks are shown at $(0, 0, \boldsymbol{Q}^*)$ and $(0, 0, -\boldsymbol{Q}^*)$. They are consequences of satellite peaks of the short-ranged conical spiral magnetic structure (see Fig. S19).

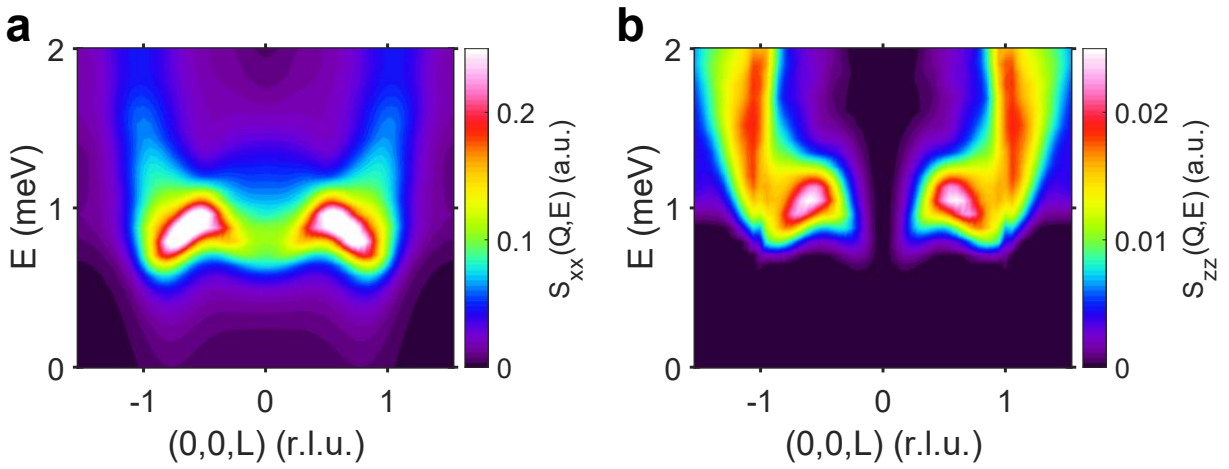

Fig. S8 | Two-spinon dynamical structure factor at zero temperature calculated by DMRG. a, Transverse dynamic structure factor $S_{xx}(\boldsymbol{Q}, E)$; **b**, Longitudinal dynamic structure factor $S_{zz}(\boldsymbol{Q}, E)$. The simulation was performed using the J_1-J_2 Hamiltonian with $J_2/|J_1| = 0.75$, $\boldsymbol{\varepsilon}_1 = 1$, and $\boldsymbol{\varepsilon}_2 = 0.425$. The values of $S_{xx}(\boldsymbol{Q}, E)$ given in the scale bar is ten times that of $S_{zz}(\boldsymbol{Q}, E)$. The anisotropic parameter $\boldsymbol{\varepsilon}_2$ causes their differences. Here the chain length is $L = 200$ sites.

It is important to clarify the definitions of reciprocal space dimensions that are used in the DMRG calculations and in the INS measurements. As shown in Fig. 1a, the lattice parameter c = 4.98985(8) Å, and the unit cell contains two spin S = 1/2 moments that are associated with magnetic orbitals. The chemical and magnetic unit cells are identical in Ti_4MnBi_2.

DMRG simulations use the length scale for individual Mn moments, i.e., $c/2$ = 2.495 Å to define the reciprocal space metric $\boldsymbol{Q}_{\text{L\_DMRG}} = 2\pi/(c/2)$. This gives the first Brillouin Zone (BZ) for DMRG as $[-2\pi/c, 2\pi/c]$, or [-2, 2] reciprocal lattice units (r.l.u) where 1 r.l.u = π/c.

INS measurements follow the convention that $\boldsymbol{Q}_{\text{L\_INS}}$ is related to the unit cell c, which contains two spin S = 1/2 moments. This gives $\boldsymbol{Q}_{\text{L\_INS}} = 1/c$, and the corresponding BZ for INS is $[-0.5/c, 0.5/c]$, or [-0.5, 0.5] r.l.u.

We use the INS BZ throughout, which involves artificially renormalizing the DMRG BZ to be consistent with the INS data.

4.3 Magnetic anisotropy in Ti_4MnBi_2: comparison of calculations and magnetization measurements

The temperature dependence of the magnetization data was measured with a 1 T field applied along the (001) and the (110) crystal directions of Ti_4MnBi_2 single crystal (Fig. S9). These data were fitted by the Curie-Weiss law:

$$\chi(T) = \frac{C}{T - \theta_{CW}} + \chi_0 \qquad (S39)$$

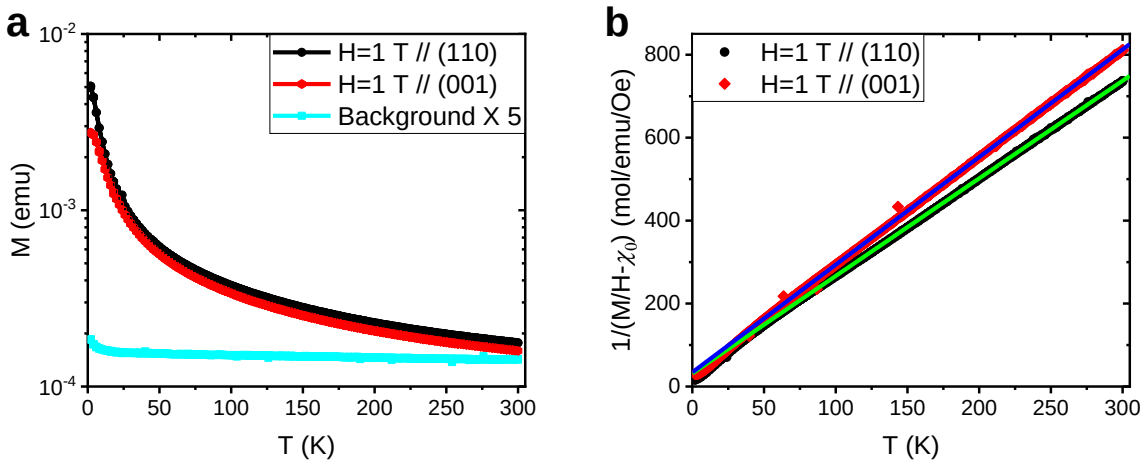

Fig. S9 | Temperature dependencies of the magnetic susceptibility in Ti_4MnBi_2. a, The magnetization as a function of temperature with a 1 T field applied along the (110) (black points) and (001) (red points) crystal directions. The signal from the empty sample holder (cyan points, multiplied by 5) is compared to the data. **b**, Corresponding plots of $[(M/H) - \chi_0]^{-1}$ with linear fits (blue and green lines) to data with temperatures larger than 50 K.

where C is the Curie constant, θ_{CW} is the paramagnetic Curie-Weiss temperature, and χ_0 is a temperature-independent susceptibility, which is likely the Pauli susceptibility expected for metallic Ti_4MnBi_2 [1] (Fig. S9). The fitted negative values of θ_{CW} are -13.3(2) K for the applied field along the (110) direction and -13.2(2) K for the applied field along the (001) direction, reflecting the net AF interaction. The fitted Curie Weiss moment is 1.843(2) μ_B/Mn for the applied field along the (110) direction and 1.756(2) μ_B/Mn for the applied field along the (001) direction. Both are close to the S = 1/2 value of 1.73 μ_B/Mn. The slight differences in the Curie-Weiss moments suggest a weak anisotropy of the Landé g-factor, whose values are close to 2.

The weak anisotropy of the single ion Landé g-factor in Ti_4MnBi_2 is proved by the loss of magnetization anisotropies at high temperatures. The magnetization data along different single crystal directions are measured by sample rotation. The sample rotates around the (001) axis for the in-plane measurements (the top panels in Fig. S10) and rotates around the (1-10) axis for the out-of-plane measurements (the bottom panels in Fig. S10). The magnetic interaction effect can be ignored at temperatures much higher than the $T_N \sim 2.0$ K [1]. The consequence is that the weak anisotropy of the magnetization at 100 K reflects the weak anisotropy of single ion Landé g-factor. Thus, the magnetization anisotropies at low temperatures come from the anisotropic magnetic interaction by assuming that the single ion Landé g-factor is temperature independent.

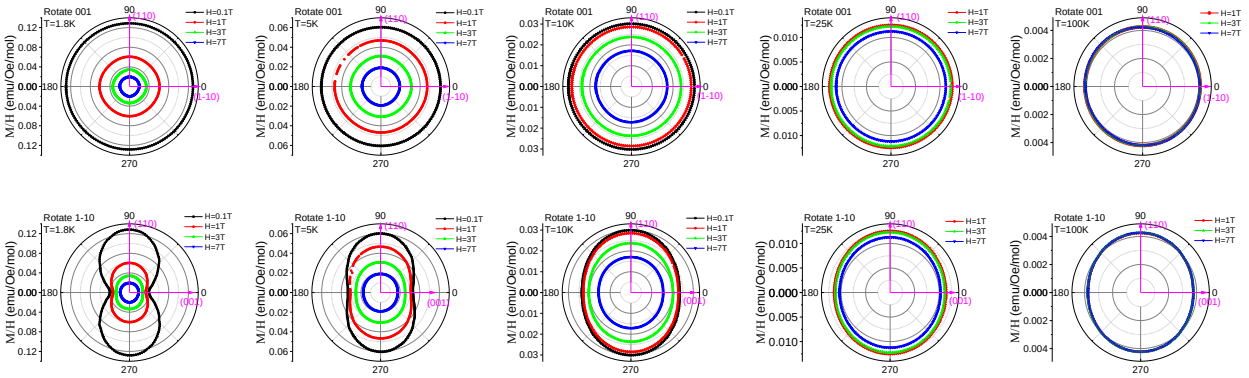

Fig. S10 | Polar plots of *M*/*H* of Ti_4MnBi_2 single crystal measured at indicated magnetic fields and temperatures. These data show that the anisotropy in the low temperature magnetization is suppressed at high temperatures, and in the presence of a magnetic field. However, 100 K and 7 T are not enough to fully suppress it. The strongest anisotropy of $(M/H)_{110}/(M/H)_{001}$ ~ 3.3 was measured at 1.8 K with 0.1 T applied magnetic field with the sample rotating around the (1-10) axis. We expect larger anisotropies to be measured at lower temperatures using smaller external magnetic fields. The measured rotation angle is reduced by 5% and shifted by 5˚ to adjust the pitch difference and sample mounting angle deviation.

The next question is whether the anisotropic magnetic interaction is an easy axis type or an easy plane type. In the case of an FM interaction, the easy axis model gives a maximum magnetization along the easy axis direction and an isotropic minimum magnetization in the plane perpendicular to the easy axis direction. The easy plane model gives an isotropic maximum magnetization in the plane, and a minimum magnetization in the direction perpendicular to the easy plane. In contrast, in the case of an AF interaction, the easy axis model gives a minimum magnetization along the easy axis direction and an isotropic maximum magnetization in the plane perpendicular to the easy axis direction; while the easy plane model gives an isotropic minimum magnetization in the plane, and a maximum magnetization in the direction perpendicular to the easy plane (Table S2). Our measured magnetization results for AF Ti_4MnBi_2 shown in Fig. S10, show a minimum magnetization along the (001) direction and a maximum isotropic magnetization in the plane perpendicular to the (001) direction, which is consistent with the results of an easy axis model, i.e., an Ising model with an Ising axis along the crystal (001) direction. This is consistent with the expectations from DFT (main text Fig. 1g).

Table S2: Different variants of magnetization anisotropy in easy-axis (Ising) and easy-plane models.

	FM	AF
Ising	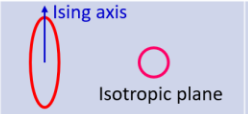	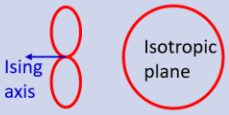
Easy-plane	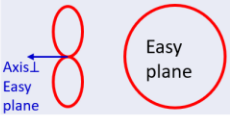	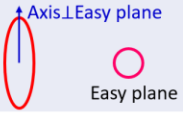

The DMRG simulation data further prove the applicability of the Ising model with an Ising axis along the (001) direction. The simulation results of a J_1-J_2 model with an Ising axis along the chain direction at zero temperature are shown in Fig. S11, roughly consistent with the low-temperature low-field experiment data shown in Fig. S10. The simulation data gives zero magnetization along the chain direction due to AF; however, the measured magnetization along the (001) direction has a non-zero minimum magnetization. This could be caused by several reasons, such as the simulation is calculated at T = 0 while experiment data is measured at temperatures higher than 1.8 K, Pauli susceptibility is not included in the simulation, a magnetic field cannot apply perfectly along the (001) direction of the sample, and the sample may have domains, etc.

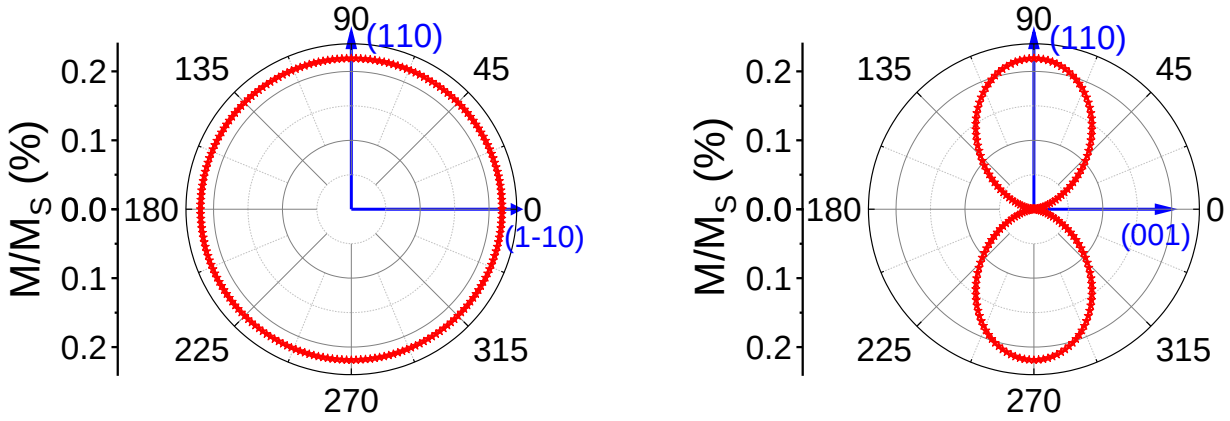

Fig. S11 | DMRG simulation of crystal rotation angle dependent magnetization in Ti_4MnBi_2 calculated at zero temperature. M_S is the saturated magnetization. The left panel is the in-plane magnetization, and the right panel is the out-of-plane magnetization. Here the chain length is L = 150 sites.

4.4 Anisotropy of the electrical resistivity ρ(T)

As a complement to the magnetization anisotropy, we have measured the anisotropy in the resistivity measured with the current along the *c*-axis (ρ_{001}) and also perpendicular to the *c*-axis (ρ_{110}). All samples were taken from a single preparation batch. The former was measured in two different samples, while the latter was measured in a single sample. The configurations of the sample leads are shown in the inset to Fig. S12a, and the measurement current was 1 mA in all cases. The temperature dependencies of all three resistivity measurements are presented in Fig. S12a. Given the size of the electrical contacts, which were made with silver-filled epoxy, and uncertainties in the geometrical factors the systematic uncertainties in the measurements are considerable. The shaded regions in Fig. S12a denote the confidence intervals for the three measurements, where ρ_{001} #1,2 are the measurements for the current along the chain axis, and ρ_{110} #3 has the current perpendicular to the chain axis.

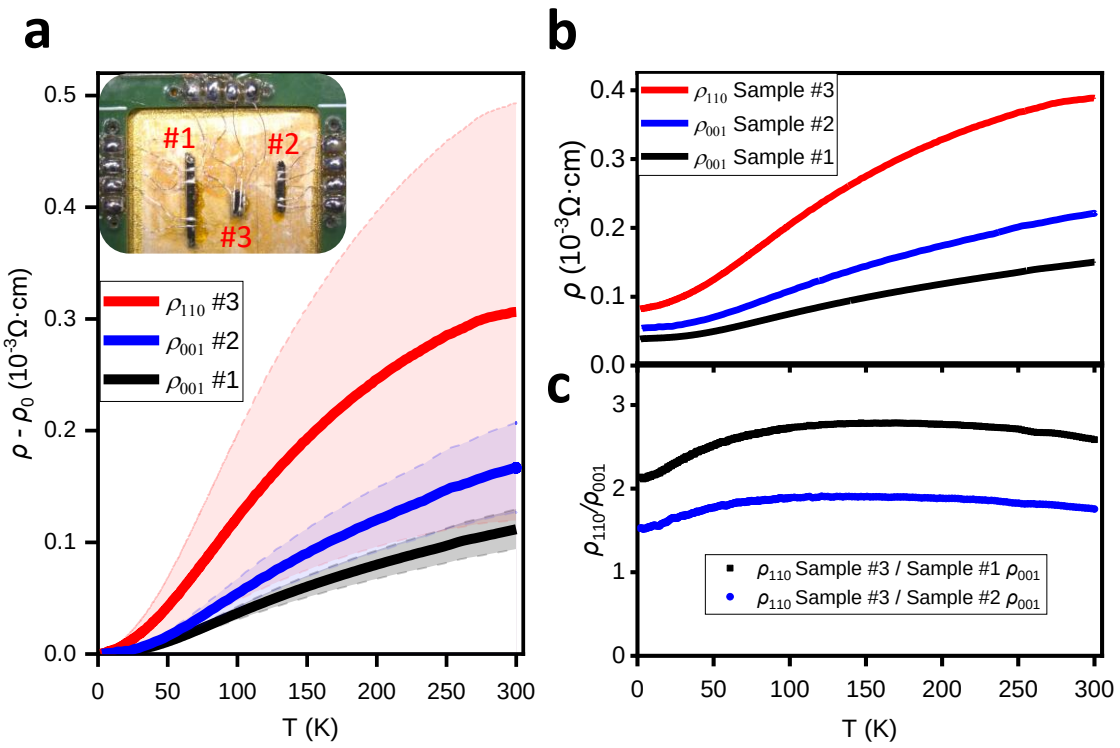

Fig. S12| Transport anisotropy. a, The temperature dependencies of the resistivity in the chain direction ρ_{001} and perpendicular to the chain direction ρ_{110}. The residual resistivities ρ_0 have been subtracted. Inset shows the contact configurations for the three crystals, where the *c*-axes are along the axis of the crystalline rods. **b**, The temperature dependencies of ρ(T) for all three samples. **c**, The temperature dependencies of the anisotropy of the resistivity ρ_{110}/ρ_{001}.

All three of these measurements display a decidedly metallic resistivity, (Fig. S12b) with very similar residual resistivity ratios RRR = 4.8 (ρ_{110}) #3, 4.2 (ρ_{001})#2, and 3.8 (ρ_{001})#1, suggesting uniform quality across the preparation batch. The resistivity anisotropy is defined as ρ_{110}/ρ_{001}, and its temperature dependencies for samples #1, #2 are presented in Fig. S12c. The anisotropy has a moderate temperature dependence of no more than ~ 25%, however, the average anisotropy is close to ~2 for both samples. This is in stark contrast to similar measurements carried out on organic conductors [31], where this anisotropy is strongly temperature dependent, and in some materials reaches values as large as 10^3-10^4. This anisotropy in the organic conductors is a consequence of the different conduction mechanisms along the stacks of organic ions, and between them, and the interplay of the relative energies related to the Mott insulating gap and the strength of the interchain coupling. As we have discussed in the main text, the chemical bonds in Ti_4MnBi_2 are much more isotropic, leading to very modest levels of resistivity anisotropy, as expected in a good metal.

This modest anisotropy in the resistivity, paired with the Fermi liquid temperature dependencies in the resistivity and the specific heat that we have reported previously [1] are together strong evidence that the conduction electrons have a three-dimensional character in Ti_4MnBi_2.

4.5 From DMRG simulation to INS experiment

DMRG calculated the transverse and longitudinal dynamic structure factors separately, while the INS experiment measured a combination of them. In the case of an isotropic Heisenberg Hamiltonian, the transverse and longitudinal dynamic structure factors are equal. However, in the case of the Ising Hamiltonian, the longitudinal dynamic structure factor will be fully suppressed. Between these two extreme cases, i.e., the Ising-like Heisenberg Hamiltonian, the relative intensity ratio $r_{L/T}$ between longitudinal and transverse dynamic structure factors depends on the anisotropy parameters $\boldsymbol{\varepsilon}_1$ and $\boldsymbol{\varepsilon}_2$. Generally, the ratio $r_{L/T}$ becomes smaller as the system becomes more Ising-like. From Eq. S5, we know that several pre-factors are added in front of the dynamic structure factor to the INS measured data, e.g., the $\boldsymbol{Q}$-dependent polarization factor, magnetic form factor, Debye-Waller factor, and some other $\boldsymbol{Q}$-independent constants (e.g., Landé g-factor, resolution volume, number of the unit cells, the classical electron radius, and the magnetic moment of the neutron). The $\boldsymbol{Q}$-independent constants can be ignored when qualitatively comparing between simulation and experiment. The Debye-Waller factor can be approximated to a unit at low temperatures, as the atomic thermal displacement should be weak. Thus, one needs to only deal with the $\boldsymbol{Q}$-dependent polarization factor and magnetic form factor. Here, we show how to get a simulation result that can be compared with the INS-measured data by adding the polarization and magnetic form factors to the DMRG calculated dynamic structure factors (Fig. S13). Note that the DMRG simulation results are calculated at zero temperature, and the INS experiment data are measured at 0.3 K (~ 1% of J_2 = 2.1 meV).

Starting from the transverse and longitudinal dynamic structure factors calculated from DMRG (Fig. S8), the unit cell of the J_1-J_2 model has one spin S = 1/2 moment along the chain while there are two spin S = 1/2 moments along the chain in the crystal structure unit cell which has been used in the INS data analysis. As explained in SI 4.2, there is a factor of four difference between the sizes of the DMRG BZ and INS BZ, calibrated in the following analysis. The polarization factors related to the experimental scattering geometry can be computed using Eq. S5 based on an Ising model. Adding these polarization factors to the DMRG-calculated dynamic structure factors produces the result shown in Fig. S13c. A comparison with the INS data reveals that the magnetic form factor governs the primary disparities. Further, using a simple Lorentzian function fitting of the INS data for small $\boldsymbol{Q}_L$ gives a reasonable estimate of the form factor. The results of adding this fitted form factor are shown in Fig. S13d. We will show the details of the calculations for the polarization and magnetic form factors in the following paragraphs.

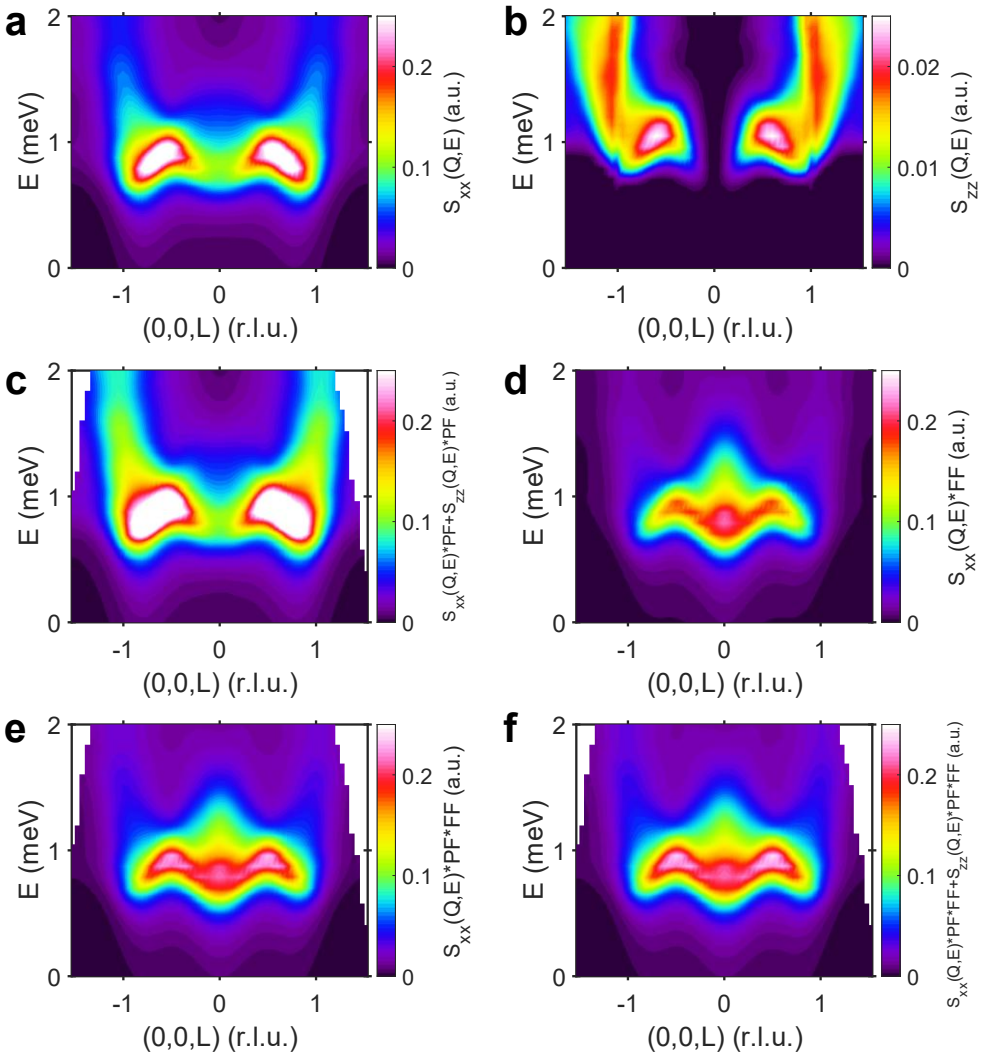

Fig. S13 | Adding polarization and magnetic form factors to the DMRG calculated magnetic dynamic structure factors. **a**, **b**, The DMRG simulated the transverse dynamic structure factor, $S^{xx}(\boldsymbol{Q}, E)$ (a), and the longitudinal dynamic structure factor, $S^{zz}(\boldsymbol{Q}, E)$ (b). Note that the scale bar of (a) is ten times of (b). **c**, The polarization factors (PF) are added to the $S^{xx}(\boldsymbol{Q}, E)$ and $S^{zz}(\boldsymbol{Q}, E)$. **d**, The Lorentzian-fitted magnetic form factor (FF) is added to the $S^{xx}(\boldsymbol{Q}, E)$. **e**, The PF of $S^{xx}(\boldsymbol{Q}, E)$ is further added to the data shown in (d). **f**, The $S^{zz}(\boldsymbol{Q}, E)$ is further added to the data shown in (e). These data should be qualitatively comparable to the INS-measured data shown in Fig. 3a. Here the chain length is L = 200 sites.

Next, we show how the neutron scattering polarization factors are calculated. The Ising-like J_1-J_2 model has been demonstrated by the crystal rotation angle-dependent magnetization data, which shows that the antiferromagnetically coupled spins align along the c-axis. In that case, the INS polarization factor can be calculated accurately using the formula $\sum_{\alpha,\beta}\left(\delta_{\alpha,\beta} - \overrightarrow{\boldsymbol{Q}_{\boldsymbol{\alpha}}} \cdot \overrightarrow{\boldsymbol{Q}_{\boldsymbol{\beta}}}\right) S^{\alpha,\beta}(\boldsymbol{Q}, E)$ for both the transverse structure factors S^{XX}, S^{YY}, and longitudinal structure factor S^{ZZ} (Fig. S14). As S^{XX} is the same as S^{YY}, their total polarization factors can be added as $(\cos^2\theta + \sin^2\theta\sin^2\varphi) + (\cos^2\theta + \sin^2\theta\cos^2\varphi) = 1+\cos^2\theta$, the polarization factor for S^{ZZ} is $\sin^2\theta$. The polarization factors added result of the combination of S^{XX}, S^{YY}, and S^{ZZ} is shown in Fig. S13c.

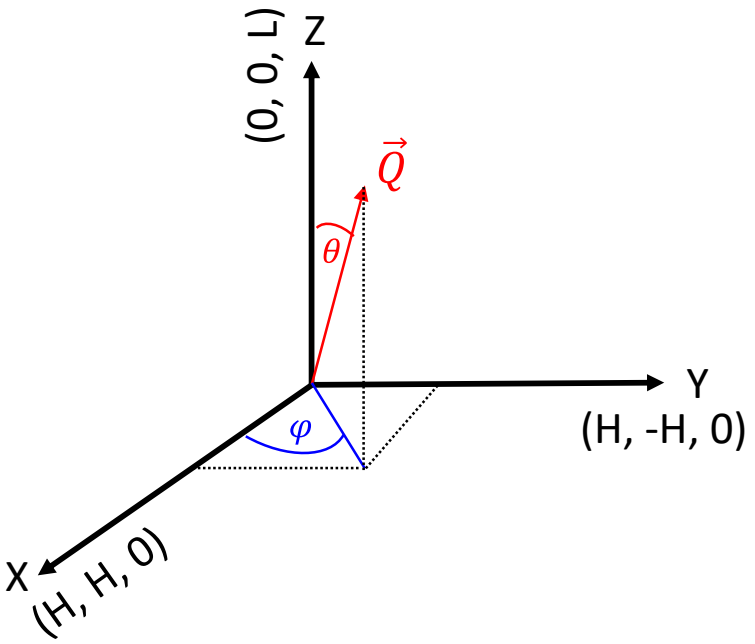

Fig. S14 | The geometry of the INS polarization factors. The Ising-axis is along the *z*-axis/(0, 0, *L*) direction.

Finally, we show how the magnetic form factor is included. Fig. S15b presents several different form factors that we considered. Figs. S15c-f are DMRG computations of $M(\boldsymbol{Q}, E)$ using these different form factors. There are two aspects of these calculations that are used to assess how well the form factors that we used reproduce the actual form factor that is realized in the sample itself. In Fig. S15c, we used the Mn^{2+} atomic form factor. It does not reproduce the strong peak in the INS data at $\boldsymbol{Q}_L = 0$, and the helimagnon [32] branches from the DMRG are hardly suppressed, indicating that this form factor falls off much too slowly with $\boldsymbol{Q}_L$. The DFT calculations are better suited for describing $M(\boldsymbol{Q}, E)$ for the large values of $\boldsymbol{Q}_L$ where the helimagnon excitations are observed in the DMRG structure factor. Fig. S15d shows the DFT form factor when the MO contains only Mn *d*-orbitals. It is clear that this form factor is an overestimate, driving the values of $M(\boldsymbol{Q}, E)$ at large $\boldsymbol{Q}$ to very low levels that are not observed in the INS data. Assuming that the MO has 70% Mn *d*-orbitals and 30% Ti *d*-orbitals results in a much better agreement (Fig. S15e), where the helimagnons are scarcely visible in the DMRG calculations, in accord with their absence in the INS data. This supports for our proposal that the $S = 1/2$ moments in Ti_4MnBi_2 originate from these MOs [19]. While the DFT form factors peaked at $\boldsymbol{Q}_L = 0$, they do not reproduce the sharpness of the fall-off found in the INS data. We fitted a Lorentzian function to the sharp fall-off in the INS data for small $\boldsymbol{Q}_L$ (Fig. S15f) with a width of W = 0.58(2) r.l.u., where 1/W = 1.72(7) l.u. is approximately two chemical cells in Ti_4MnBi_2. This suggests that the magnetization density that scatters the neutrons is extended along the chain and falls off more gradually in the transverse direction, similar to the Mn^{2+} atomic form factor. This phenomenological form factor underestimates the form factor at larger $\boldsymbol{Q}_L$, as clear signatures of the helimagnons are evident that are absent in the INS data. Nevertheless, except where indicated otherwise, we will use the Lorentzian form factor.

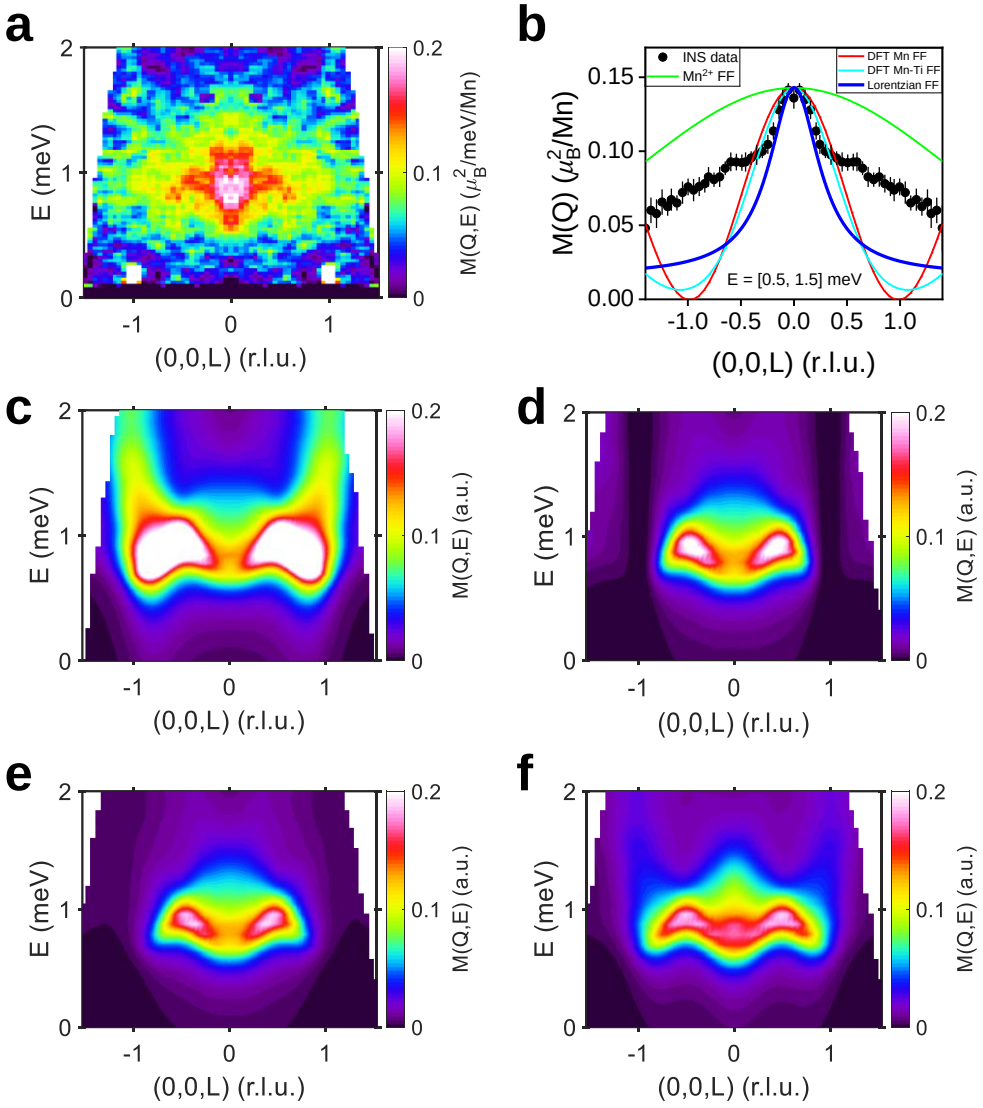

Fig. S15 | Magnetic form factor in Ti_4MnBi_2. **a**, The INS data for $M(\boldsymbol{Q}, E)$. **b**, Different form factors (FF) compared to the INS data. **c**, DMRG calculation of $M(\boldsymbol{Q}, E)$ using the Mn^{2+} FF. **d**, DMRG calculation using DFT FF with only Mn *d*-orbital weight in the MO. **e**, Same as (d), but with 70% Mn *d*-orbital and 30% Ti *d*-orbital admixture. **f**, DMRG calculation of $M(\boldsymbol{Q}, E)$ using a Lorentzian FF. Here the chain length is L = 200 sites.

4.6 Inelastic neutron scattering and the parameters of the J_1-J_2 XXZ model

The parameters of the J_1-J_2 XXZ model $\boldsymbol{\alpha} = J_2/|J_1|$ and $\boldsymbol{\varepsilon}_2$ are determined by comparing the DMRG calculations to the INS measurements, with the optimal result in Fig. S16. Forty-two different DMRG simulations were carried out, with $0.5 \leq \boldsymbol{\alpha} \leq 2$ and $0 \leq \boldsymbol{\varepsilon}_2 \leq 0.5$, with $\boldsymbol{\varepsilon}_1 = 1$ throughout. Examples of the computed magnetic dynamical structure factor are shown for different values of $\boldsymbol{\alpha}$ and $\boldsymbol{\varepsilon}_2$ in Fig. S17. The comparisons between the most dispersing parts of the INS spinon spectra and the DMRG spectra are shown in Fig. S18, from which the optimal parameters of $\boldsymbol{\alpha}$ = 0.75(5) and $\boldsymbol{\varepsilon}_2$ = 0.43(3) have been selected, and are used throughout this work.

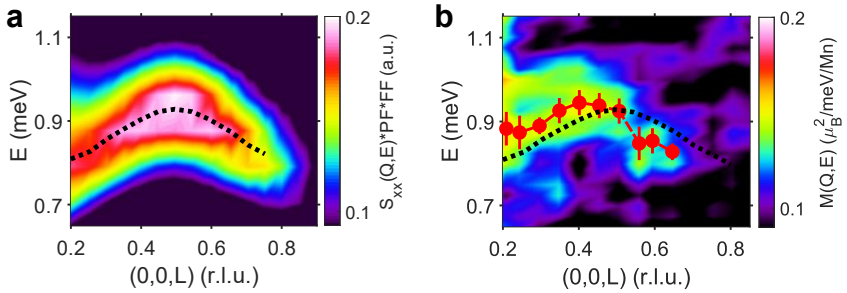

Fig. S16 | Spinon dispersions in DMRG and INS data in Ti_4MnBi_2. The most sensitive determination of the parameters for the J_1-J_2 XXZ model compares the spinon dispersions from DMRG to the dispersion measured by INS. **a**, The DMRG calculated the transverse dynamic structure factors, $S_{xx}(\boldsymbol{Q}, E)$, with $\alpha = J_2/|J_1| = 0.75$ and $\varepsilon_2 = 0.425$. The polarization factor (PF) and form factor (FF) are added to compare the INS data. The red circles indicate the spinon dispersion from the INS measurements in **b**. The black dot lines are the spinon dispersion from the DMRG simulation in (a). Here the chain length is $L = 200$ sites.

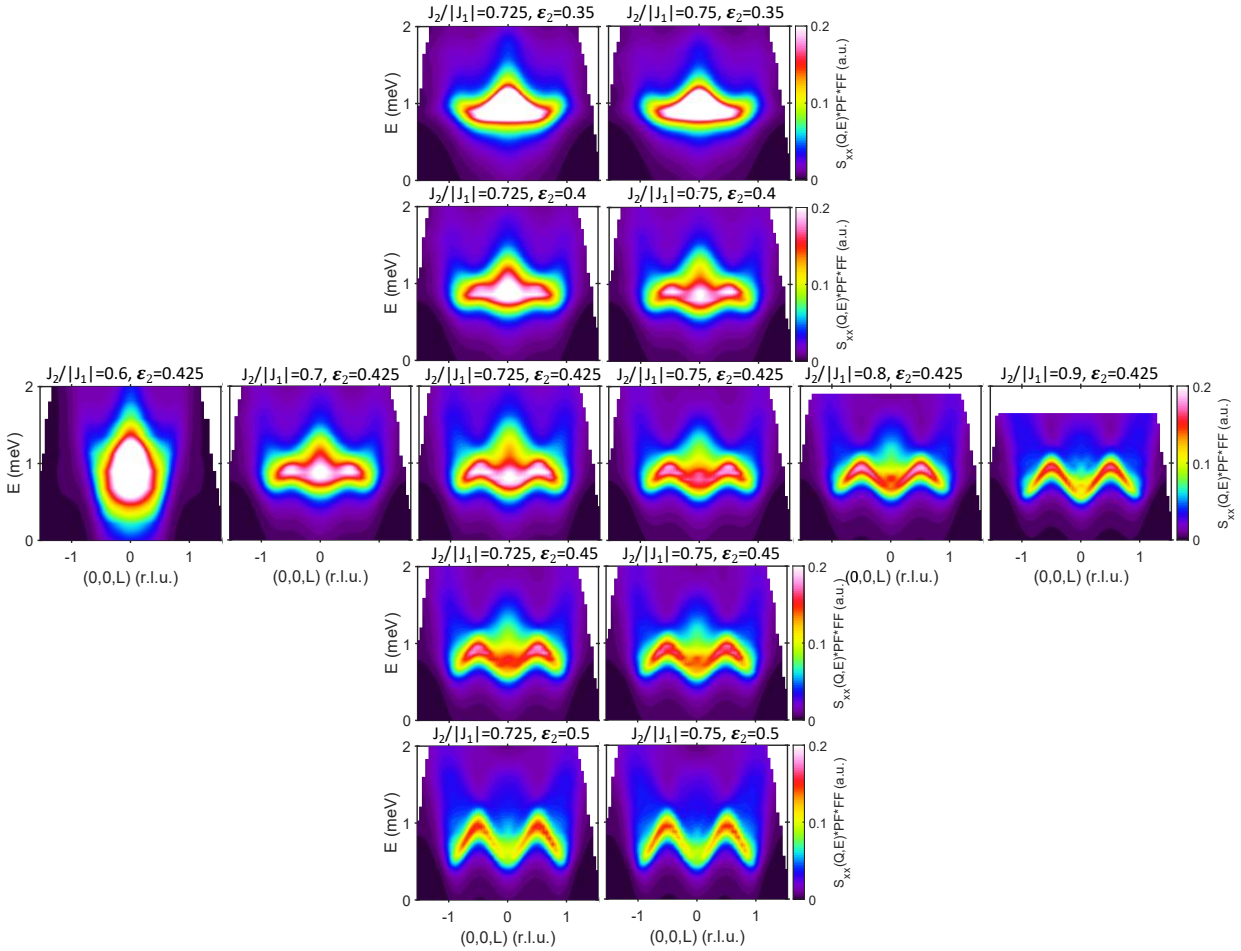

Fig. S17 | The complete magnetic dynamic structure factors from DMRG for different values of parameters $\alpha = J_2/|J_1|$ and ε_2 from the J_1-J_2 XXZ model. The panel with $\alpha = 0.6$, $\varepsilon_2 = 0.425$ is the only one in the ungapped FM phase, while the others are in either the ↑↓↑↓ phase or vector chiral (VC) phase. Qualitatively, the INS date that most resemble the structure factors appear near the center of the figure. Here the chain length is $L = 200$ sites.

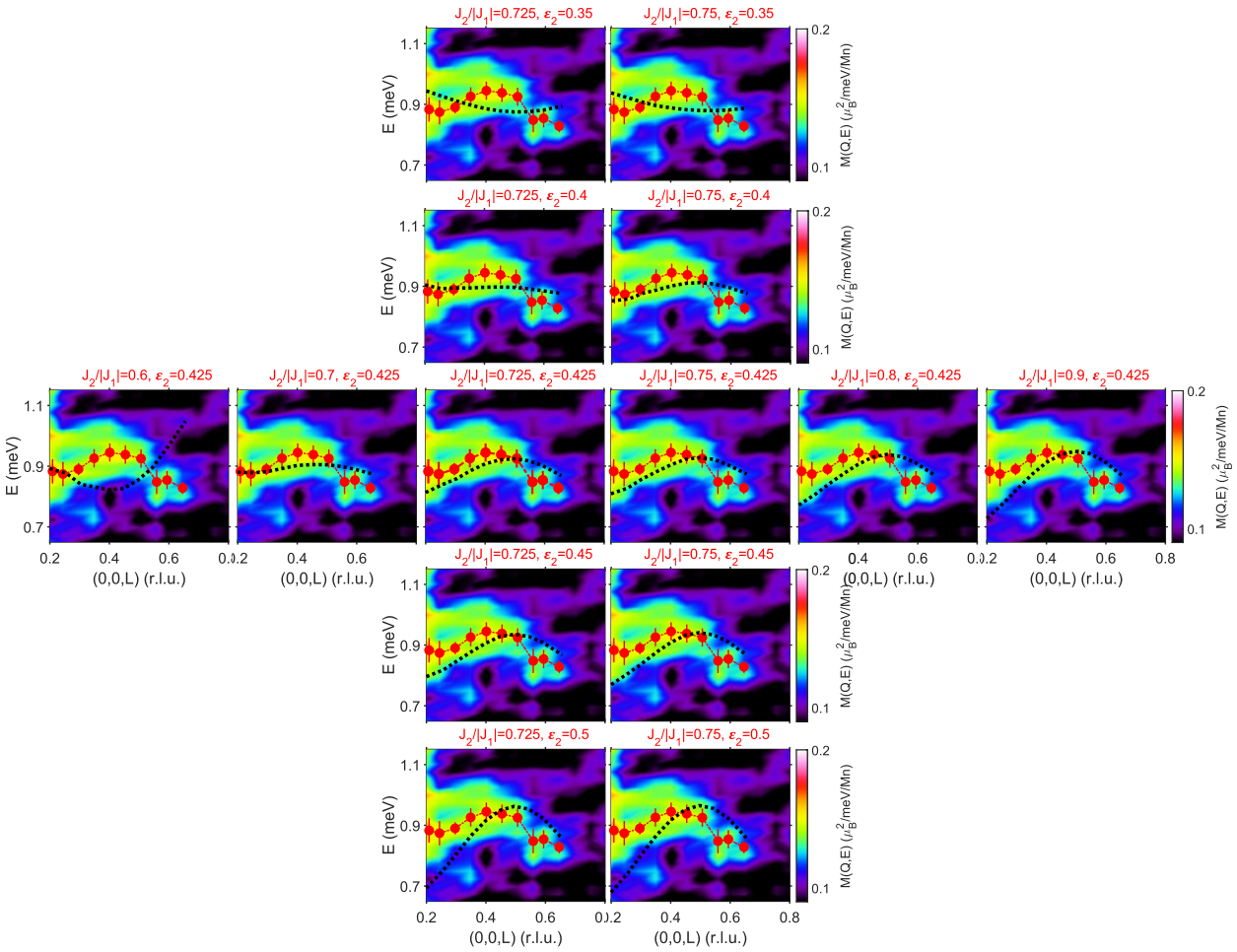

Fig. S18 | Parameterizing the INS spinon spectrum. Shown is a closeup of the spinon spectrum from the INS measurements, overlaid with the spinon spectrum calculated by DMRG for a number of different values of $\alpha = J_2/|J_1|$ and ε_2. The red circles indicate the spinon dispersion from the INS measurements. The black dot lines are the spinon dispersion from the DMRG simulations with α and ε_2 values indicated. The best agreement is obtained for $0.7 < \alpha < 0.8$, and for $0.4 < \varepsilon_2 < 0.45$ which roughly provides the confidence limits. Based on this comparison, we have chosen $\alpha = 0.75(5)$ and $\varepsilon_2 = 0.43(3)$ as the optimal parameters for Ti_4MnBi_2.

5. Spinon Propagation in the $S = 1/2$ J_1-J_2 XXZ Chain

The underlying state for the spinons in the J_1-J_2 FM XXZ chain is ↑↑↓↓, with first neighbors coupled by the FM exchange J_1 and second neighbors by the AF exchange J_2. Figure S19 shows how a single spin flip ($\Delta S = 1$, $\Delta E = 2J_2$) subsequently creates domain walls (spinons) and how they propagate by reversing additional spins. Second step of the spinon propagation creates an energy difference $\Delta E = 2J_2 - 2|J_1|$, which is negative when $J_2 < |J_1|$. Subsequent spin flips cost zero energy, as is the case for the conventional ↑↓↑↓ XXZ chain, where a pair of spinons propagate freely.

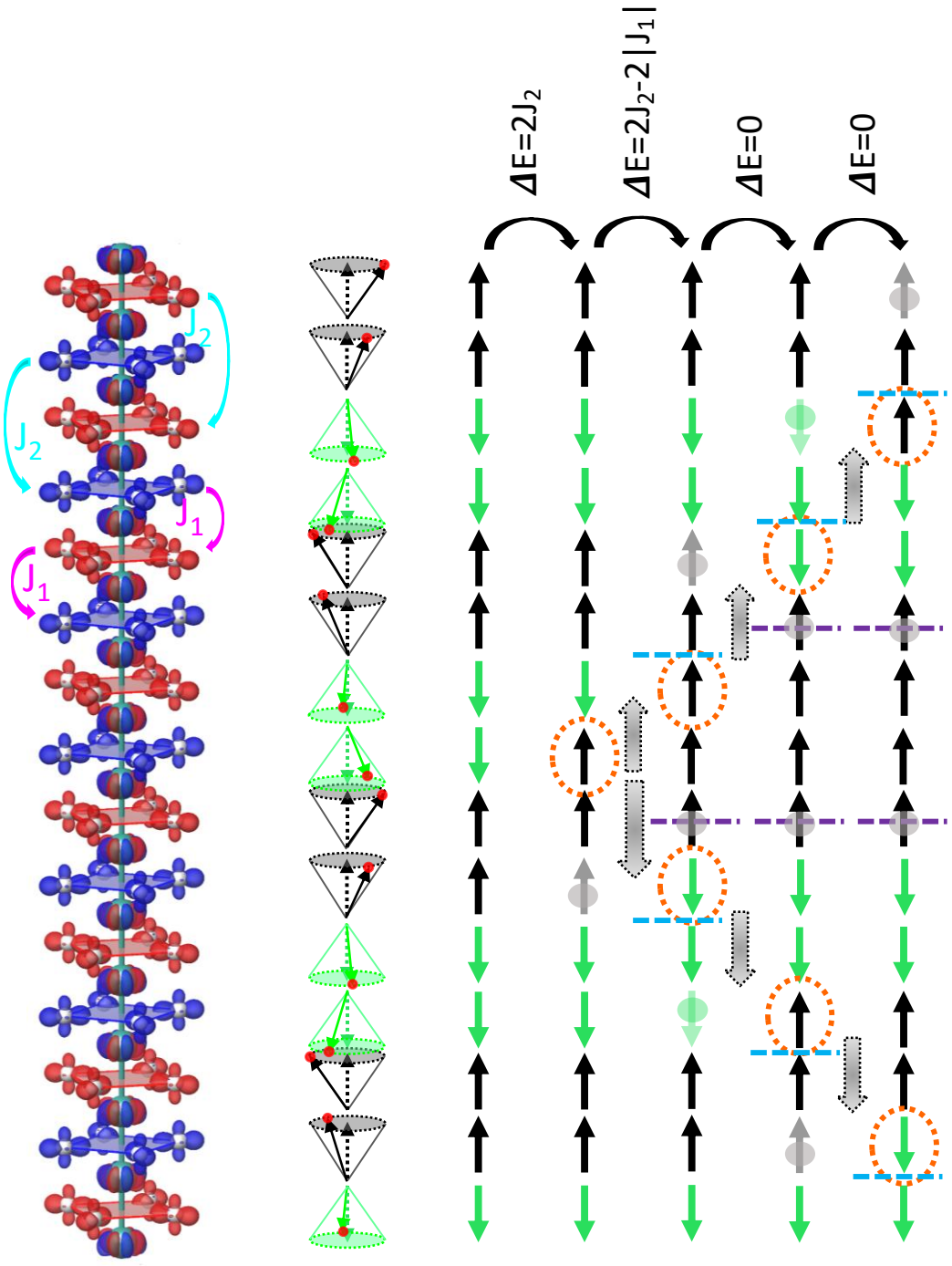

Fig. S19 | Spin configuration and spinon propagation in an ↑↑↓↓ spin *S* = 1/2 chain. The MO configurations that provide the moments are indicated in the leftmost column (for more information see Fig. 1 and related text), resulting in the conical spiral spin configuration shown in the second column. Column 3 is the underlying ↑↑↓↓ spin configuration along the chain direction, column 4 depicts a single spin flip that subsequently generates a pair of spinons in column 5. Columns 6 and 7 show subsequent steps in the spinon propagation. Unlike the conventional ↑↓↑↓ AF spin chain, in the J_1-J_2 XXZ chain there are single domain walls accompanied by spinon propagation (the spins that are marked by filled circles).

6. Low Energy Excitations: a comparison of AMATERAS and DNA measurements

Since both AMATERAS and DNA data are calibrated to the absolute units (see SI 2.2), one can plot the AMATERAS and DNA data together. The $M(E)$ data shown in Fig. 4a are the powder averaged data of the full 180˚ rotation angle data, averaged over Q space [1.1, 1.5] $Å^{-1}$ to avoid the Bragg peaks where elastic broadening usually contaminates the quasielastic signal. The data are shown in raw data plots without any background subtraction. The 0.3 K DNA data (solid black squares) serves as a background level reflecting the incoherent elastic nuclear scattering, with the black dash line being an elastic line convolved with instrumental resolution. The insert data present the $\chi''(E)$ measured at 1, 2, and 5 K with this 0.3 K background subtracted.

7. Temperature Dependencies of $M(Q, E)$ and $\chi''(E)$

The INS measured magnetic dynamic structure factor $M(\boldsymbol{Q}, E)$ and the imaginary part of the dynamical magnetic susceptibility $\chi''(\boldsymbol{Q}, E)$ 2D plots are shown for different temperatures in Fig. S20.

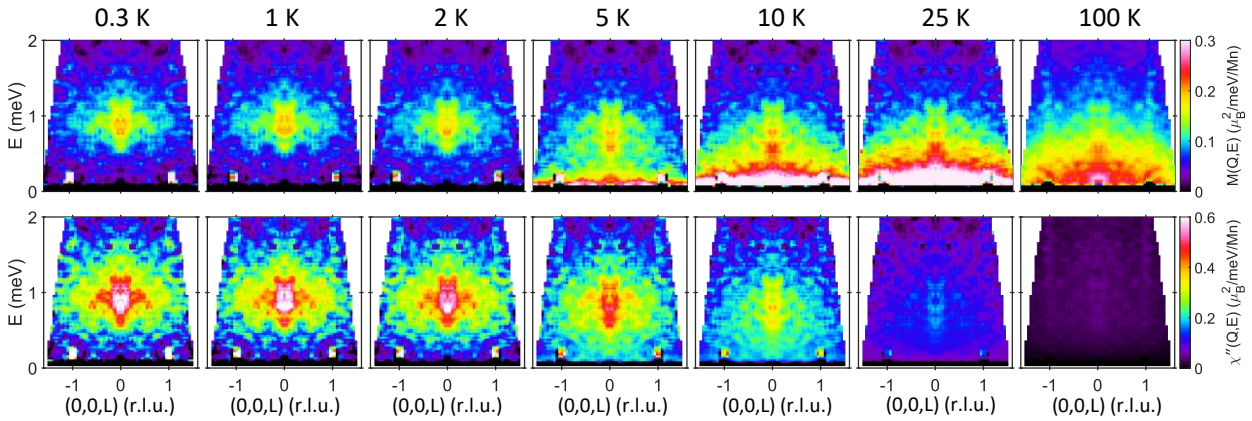

Fig. S20 | Temperature dependence of the INS measured magnetic dynamic structure factor $M(Q, E)$ and the corresponding dynamical magnetic susceptibility $\chi''(Q, E)$ in Ti_4MnBi_2. The data are measured at 0.3, 1, 2, 5, 10, 25, and 100 K using AMATERAS@J-PARC.

We plotted the magnetic dynamic susceptibility data, $\chi''(\boldsymbol{Q}, E)$, in different scale bars (top row, bottom row) and compared them in Fig. S21. While there is evidently considerable temperature dependence to these data, it is clear that the spinons contribute significantly to $\chi''(\boldsymbol{Q}, E)$, even at 100 K.

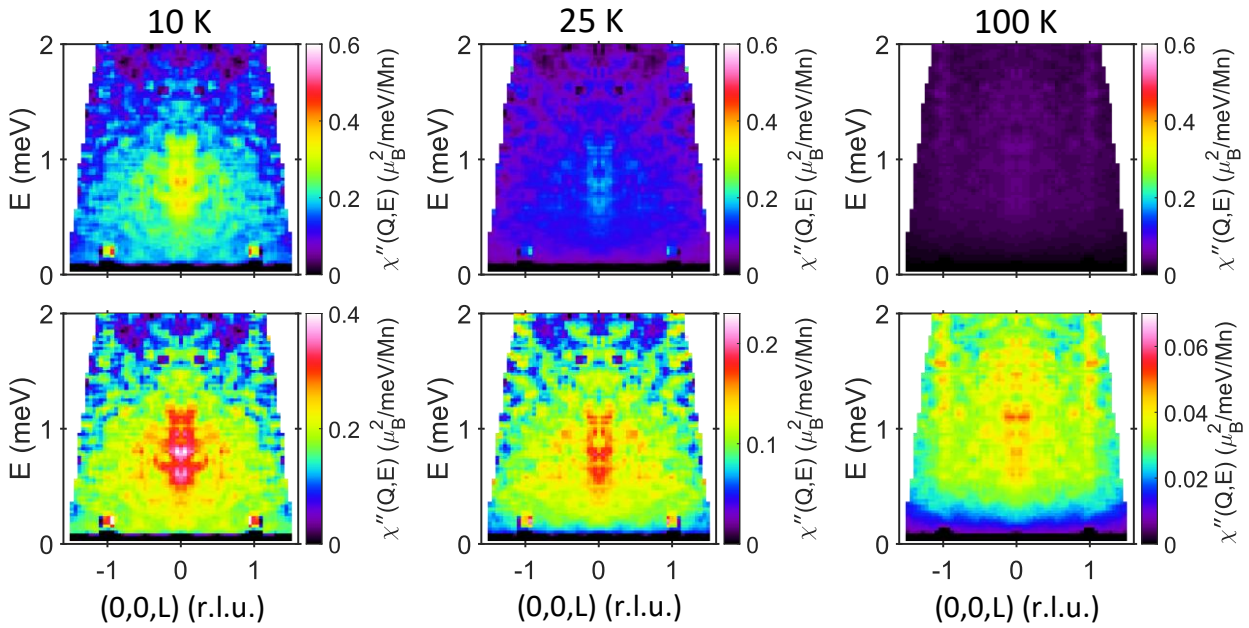

Fig. S21 | Temperature dependence of the INS measured dynamical magnetic susceptibility in Ti_4MnBi_2. The top panels are the $\chi''(\boldsymbol{Q}, E)$ plots at indicated temperatures, and the bottom panels are the same data plotted with an adjusted color bar.

8. J_1-J_2 XXZ Materials

A list of known materials described by the S = 1/2 FM J_1-J_2 XXZ chain are presented in Table S3 and Fig. S22.

Table S3. Materials described by the S = 1/2 FM Chain J_1-J_2 XXZ model.

	J_1/meV	J_2/meV	$\alpha = J_2/J_1$	$\mathcal{E}_1$	$\mathcal{E}_2$	Type/References	
β-$TeVO_4$	-3.3	3.3	-1	0.9	1.1	--	[33]
$NaCuMoO_4(OH)$	-4.4	3.1	-0.71	1	1	Isotropic	[34]
$Ca_2Y_2Cu_5O_{10}$	-14.6	2.8	-0.19	1	1	Isotropic	[35]
$Ca_2Y_2Cu_5O_{10}$	-24	5.5	-0.23	1	1	Isotropic	[36]
$LiCuVO_4$	-2.4	3.4	-1.4	1	1	Isotropic	[37]
$LiCuVO_4$	-1.6	5.59	-3.5	1	1	Isotropic	[38]
Li_2CuO_2	-18.7	5.8	-0.32	0.98	1	Ising	[39]
Li_2CuO_2	-8.6	5.3	-0.62	1	1	Isotropic	[40]
Li_2ZrCuO_4	-27	7.8	-0. 3	1	1	Isotropic	[41]
$PbCuSO_4(OH)_2$	-9.8	2.6	-0.27	1	1	Isotropic	[42]
$PbCuSO_4(OH)_2$	-9.8	3.2	-0.33	1	1	Isotropic	[43]
$LiCuSbO_4$	-6.5	2.9	-0.45	1.2	1	Easy plane	[44]
$Rb_2Cu_2Mo_3O_{12}$	-11.9	4.4	-0.37	1	1	Isotropic	[45]
$La_6Ca_8Cu_{24}O_{41}$	-18.5	6.7	-0.36	1	1	Isotropic	[40]
$LiCu_2O_2$	-11	7	-0.64	1	1	Isotropic	[46]
$CoNb_2O_6$	-2.8	0.42	-0.15	0.24	0	Ising	[47]
Ti_4MnBi_2	-2.8	2.1	-0.75	1	0.425	Ising	(This work)

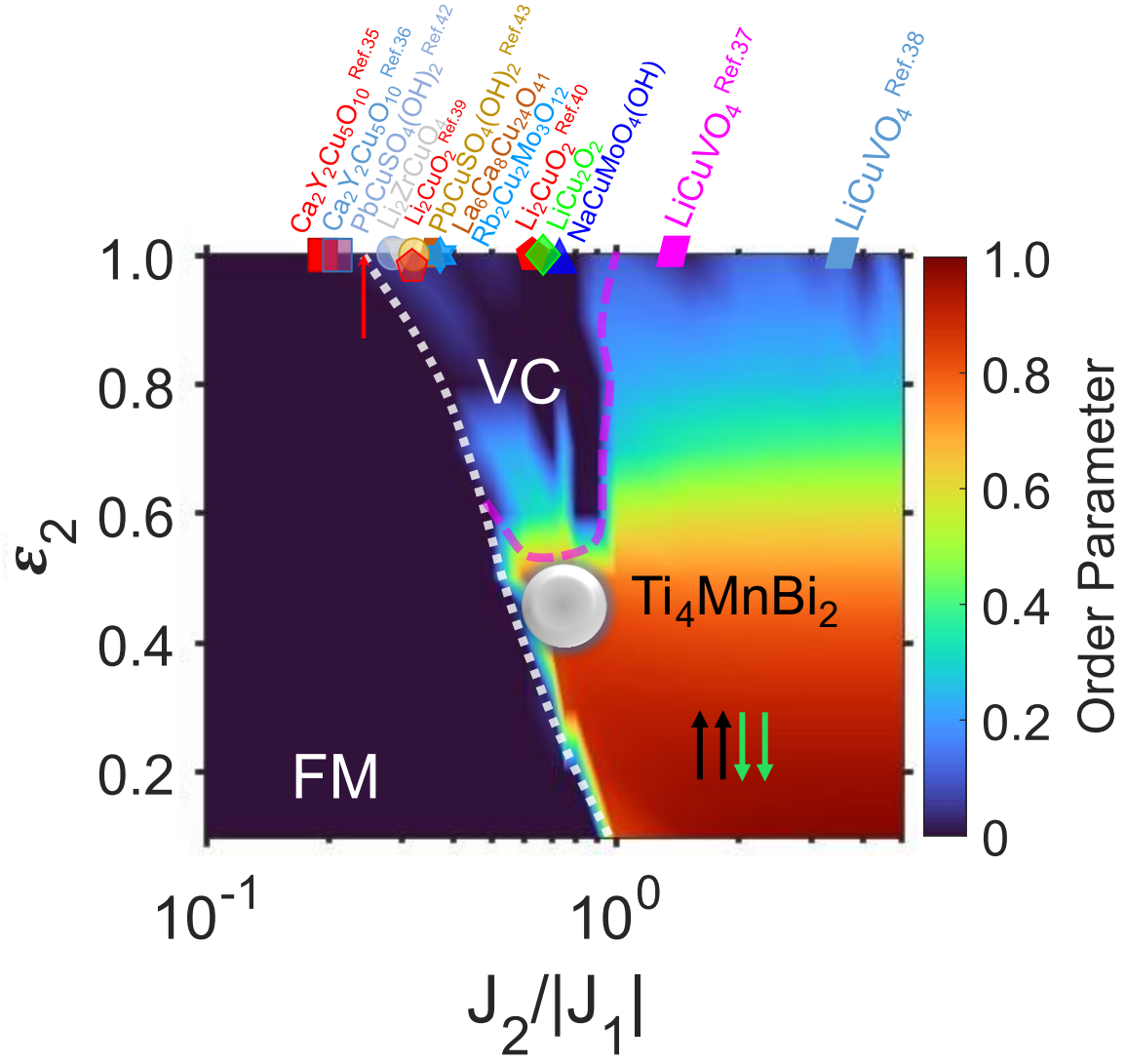

Fig. S22 | The materials from Table S3 are placed on the phase diagram of the J_1-J_2 XXZ model (Fig. 1h). Ti_4MnBi_2 is singular among these materials, not only for being the only metal, but also because of its pronounced Ising (easy-axis) anisotropy. The red arrow pointed the critical value of $J_2/|J_1| = 0.25$ for an isotropic Heisenberg J_1-J_2 model.

Supplementary References

1. Pandey, A. *et al.* Correlations and incipient antiferromagnetic order within the linear Mn chains of metallic Ti_4MnBi_2. *Phys. Rev. B* **102**, 014406 (2020).
2. Richter, C. G., Jeitschko, W., Künnen, B. & Gerdes, M. H. The Ternary Titanium Transition Metal Bismuthides Ti_4TBi_2 with T = Cr, Mn, Fe, Co, and Ni. *J. Solid State Chem.* **133**, 400–406 (1997).
3. Rytz, R. & Hoffmann, R. Chemical bonding in the ternary transition metal bismuthides Ti_4TBi_2 with T = Cr, Mn, Fe, Co, and Ni. *Inorg. Chem.* **38**, 1609–1617 (1999).
4. Rule, K. C., Mole, R. A. & Yu, D. Which glue to choose? A neutron scattering study of various adhesive materials and their effect on background scattering. *J. Appl. Crystallogr.* **51**, 1766–1772 (2018).
5. Nakajima, K. *et al.* AMATERAS: A Cold-Neutron Disk Chopper Spectrometer. *J. Phys. Soc. Japan* **80**, SB028 (2011).
6. Inamura, Y., Nakatani, T., Suzuki, J. & Otomo, T. Development Status of Software "Utsusemi" for Chopper Spectrometers at MLF, J-PARC. *J. Phys. Soc. Japan* **82**, SA031 (2013).
7. Azuah, R. T. *et al.* DAVE: A Comprehensive Software Suite for the Reduction, Visualization, and Analysis of Low Energy Neutron Spectroscopic Data. *J. Res. Natl. Inst. Stand. Technol.* **114**, 341-358 (2009).
8. Kawakita, Y. *et al.* Recent Progress on DNA ToF Backscattering Spectrometer in MLF, J-PARC. *EPJ Web Conf.* **272**, 02002 (2022).
9. Wu, L. S. *et al.* Orbital-exchange and fractional quantum number excitations in an f-electron metal, Yb_2Pt_2Pb. *Science* **352**, 1206–1210 (2016).
10. More information about the absorption Correction is on the Mantid website: (available at https://docs.mantidproject.org/v6.1.0/concepts/AbsorptionAndMultipleScattering.html).
11. Sears, V. F. Neutron scattering lengths and cross sections. *Neutron News* **3**, 26–37 (1992).
12. Xu, G., Xu, Z. & Tranquada, J. M. Absolute cross-section normalization of magnetic neutron scattering data. *Rev. Sci. Instrum.* **84**, 083906 (2013).
13. Hong, T. *et al.* Neutron scattering from a coordination polymer quantum paramagnet. *Phys. Rev. B* **74**, 094434 (2006).
14. Enderle, M. Neutrons and magnetism. *École thématique la Société Française la Neutron.* **13**, 01002 (2014).
15. Price, D. L. & Fernandez-Alonso, F. An Introduction to Neutron Scattering. in *Experimental Methods in the Physical Sciences* vol. 44 1–136 (Elsevier Inc., 2013).
16. Schröder, A. *et al.* Onset of antiferromagnetism in heavy-fermion metals. *Nature* **407**, 351–355 (2000).
17. Blaha, P. *et al.* WIEN2k: An APW+lo program for calculating the properties of solids. *J. Chem. Phys.* **152**, 074101 (2020).
18. Perdew, J. P., Burke, K. & Ernzerhof, M. Generalized Gradient Approximation Made Simple. *Phys. Rev. Lett.* **77**, 3865–3868 (1996).
19. Jin, Z. *et al.* Magnetic molecular orbitals in MnSi. *Sci. Adv.* **9**, eadd5239 (2023).
20. Anisimov, V. I., Zaanen, J. & Andersen, O. K. Band theory and Mott insulators: Hubbard U instead of Stoner I. *Phys. Rev. B* **44**, 943–954 (1991).
21. Foyevtsova, K. & Sawatzky, G. A. A Band Theory Perspective on Molecular Orbitals in Complex Oxides. *J. Mod. Phys.* **10**, 953–965 (2019).
22. Ganner, T. Sommerfeld expansion for various metals. (Technischen Universitat Graz, 2010).
23. White, S. R. Density matrix formulation for quantum renormalization groups. *Phys. Rev.*

Lett. **69**, 2863–2866 (1992).
24. Schollwöck, U. The density-matrix renormalization group in the age of matrix product states. *Ann. Phys.* **326**, 96–192 (2011).
25. Alvarez, G. The density matrix renormalization group for strongly correlated electron systems: A generic implementation. *Comput. Phys. Commun.* **180**, 1572–1578 (2009).
26. Furukawa, S., Sato, M. & Onoda, S. Chiral Order and Electromagnetic Dynamics in One-Dimensional Multiferroic Cuprates. *Phys. Rev. Lett.* **105**, 257205 (2010).
27. Heidrich-Meisner, F., Honecker, A. & Vekua, T. Frustrated ferromagnetic spin-1/2 chain in a magnetic field: The phase diagram and thermodynamic properties. *Phys. Rev. B* **74**, 020403(R) (2006).
28. Sirker, J. Thermodynamics of multiferroic spin chains. *Phys. Rev. B* **81**, 014419 (2010).
29. Nocera, A. & Alvarez, G. Spectral functions with the density matrix renormalization group: Krylov-space approach for correction vectors. *Phys. Rev. E* **94**, 053308 (2016).
30. Nocera, A. & Alvarez, G. Root-*N* Krylov-space correction vectors for spectral functions with the density matrix renormalization group. *Phys. Rev. B* **106**, 205106 (2022).
31. Jerome, D. & Bourbonnais, C. Quasi one-dimensional organic conductors: from Fröhlich conductivity and Peierls insulating state to magnetically-mediated superconductivity, a retrospective. *Comptes Rendus Phys.* **25**, 17–178 (2024).
32. Ren, J. & Sirker, J. Spinons and helimagnons in the frustrated Heisenberg chain. *Phys. Rev. B* **85**, 140410(R) (2012).
33. Pregelj, M. *et al.* Coexisting spinons and magnons in the frustrated zigzag spin-1/2 chain compound β-$TeVO_4$. *Phys. Rev. B* **98**, 094405 (2018).
34. Nawa, K. *et al.* $NaCuMoO_4(OH)$ as a candidate frustrated J_1-J_2 Chain Quantum Magnet. *J. Phys. Soc. Japan* **83**, 103702 (2014).
35. Kuzian, R. O. *et al.* $Ca_2Y_2Cu_5O_{10}$: The first frustrated quasi-1d ferromagnet close to criticality. *Phys. Rev. Lett.* **109**, 117207 (2012).
36. Matsuda, M. *et al.* Highly dispersive magnons with spin-gap-like features in the frustrated ferromagnetic S = 1/2 chain compound $Ca_2Y_2Cu_5O_{10}$ detected by inelastic neutron scattering. *Phys. Rev. B* **100**, 104415 (2019).
37. Enderle, M. *et al.* Two-spinon and four-spinon continuum in a frustrated ferromagnetic spin-1/2 chain. *Phys. Rev. Lett.* **104**, 237207 (2010).
38. Enderle, M. *et al.* Quantum helimagnetism of the frustrated spin-1/2 chain $LiCuVO_4$. *Europhys. Lett.* **70**, 237–243 (2005).
39. Zoghlin, E., Stone, M. B. & Wilson, S. D. Refined spin-wave model and multimagnon bound states in Li_2CuO_2. *Phys. Rev. B* **108**, 064408 (2023).
40. Mizuno, Y. *et al.* Electronic states and magnetic properties of edge-sharing Cu-O chains. *Phys. Rev. B* **57**, 5326–5335 (1998).
41. Drechsler, S. L. *et al.* Frustrated cuprate route from antiferromagnetic to ferromagnetic spin-1/2 heisenberg chains: Li_2ZrCuO_4 as a missing link near the quantum critical point. *Phys. Rev. Lett.* **98**, 077202 (2007).
42. Heinze, L. *et al.* Low-energy spin excitations of the frustrated ferromagnetic J_1-J_2 chain material linarite $PbCuSO_4(OH)_2$ in applied magnetic fields parallel to the *b* axis. *Phys. Rev. B* **106**, 144409 (2022).
43. Rule, K. C. *et al.* Dynamics of linarite: Observations of magnetic excitations. *Phys. Rev. B* **95**, 024430 (2017).
44. Dutton, S. E. *et al.* Quantum spin liquid in frustrated one-dimensional $LiCuSbO_4$. *Phys. Rev. Lett.* **108**, 187206 (2012).
45. Hase, M. *et al.* Magnetic properties of $Rb_2Cu_2Mo_3O_{12}$ including a one-dimensional spin-

1/2 Heisenberg system with ferromagnetic first-nearest-neighbor and antiferromagnetic second-nearest-neighbor exchange interactions. *Phys. Rev. B* **70**, 104426 (2004).
46. Park, S., Choi, Y. J., Zhang, C. L. & Cheong, S. W. Ferroelectricity in an S = 1/2 chain cuprate. *Phys. Rev. Lett.* **98**, 057601 (2007).
47. Fava, M., Coldea, R. & Parameswaran, S. A. Glide symmetry breaking and Ising criticality in the quasi-1D magnet $CoNb_2O_6$. *Proc. Natl. Acad. Sci. U. S. A.* **117**, 25219–25224 (2020).